

PLASMROID INSTABILITY IN EVOLVING CURRENT SHEETS AND ONSET OF FAST RECONNECTION

YI-MIN HUANG,¹ LUCA COMISSO,¹ AND A. BHATTACHARJEE¹

¹*Department of Astrophysical Sciences, Princeton Plasma Physics Laboratory, Princeton Center for Heliophysics, and Max Planck/Princeton Center for Plasma Physics, Princeton University, Princeton, New Jersey 08543, USA*

Abstract

The scaling of plasmoid instability maximum linear growth rate with respect to Lundquist number S in a Sweet-Parker current sheet, $\gamma_{max} \sim S^{1/4}$, indicates that at high S , the current sheet will break apart before it approaches the Sweet-Parker width. Therefore, a proper description for the onset of the plasmoid instability must incorporate the evolving process of the current sheet. We carry out a series of two-dimensional simulations and develop diagnostics to separate fluctuations from an evolving background. It is found that the fluctuation amplitude starts to grow only when the linear growth rate is sufficiently large ($\gamma_{max}\tau_A > O(1)$) to overcome advection loss and the stretching effect due to the outflow. The linear growth rate continues to rise until the sizes of plasmoids become comparable to the inner layer width of the tearing mode. At this point the current sheet is disrupted and the instability enters the early nonlinear regime. The growth rate suddenly decreases, but the reconnection rate starts to rise rapidly, indicating that current sheet disruption triggers the onset of fast reconnection. We identify important time scales of the instability development, as well as scalings for the linear growth rate, current sheet width, and dominant wavenumber at disruption. These scalings depend on not only the Lundquist number, but also the noise amplitude. A phenomenological model that reproduces scalings from simulation results is proposed. The model incorporates the effect of reconnection outflow, which is crucial for yielding a critical Lundquist number S_c below which disruption does not occur. The critical Lundquist number S_c is not a constant value but has a weak dependence on the noise amplitude.

arXiv:1707.01863v2 [physics.plasm-ph] 3 Oct 2017

1. INTRODUCTION

Most of the visible universe is in plasma state, where the presence of magnetic field is ubiquitous. At large spatial and slow temporal scales relative to kinetic scales, the dynamics of highly conducting magnetized plasmas is governed by ideal magnetohydrodynamics (MHD) equations. A topological constraint imposed by ideal MHD is the frozen-in condition, which implies the preservation of field line connectivity among fluid elements (Alfvén 1943). Magnetic reconnection is a fundamental process that allows plasmas to break free from the frozen-in constraint, thereby enabling the conversion of magnetic energy to plasma energy. Magnetic reconnection is generally believed to be the underlying mechanism that powers explosive events in nature, such as magnetospheric substorms, solar flares, coronal mass ejections (CME), gamma-ray bursts, and sawtooth crashes in fusion plasmas (see Biskamp 2000; Priest & Forbes 2000; Zweibel & Yamada 2009; Yamada et al. 2010; Zweibel & Yamada 2016, for recent reviews).

Magnetic reconnection events in nature are often preceded by an extended quiescent period and then an impulsive “onset” phase. During the onset phase the reconnection rate increases abruptly, and subsequently reconnection proceeds rapidly after the onset (Bhattacharjee 2004; Cassak et al. 2005). Accordingly, a successful theory of reconnection must account for not only the observed fast reconnection rate, but also the impulsive onset. The classical Sweet-Parker theory (Parker 1957; Sweet 1958) based on resistive MHD fails to accomplish both tasks. The Sweet-Parker theory assumes that reconnection takes place in an extended current sheet of length L , which is determined by the global configuration. The governing dimensionless parameter of the system is the Lundquist number $S \equiv V_A L / \eta$, where V_A is the Alfvén speed of the reconnecting magnetic field and η is the magnetic diffusivity. The theory predicts that the width of the current sheet scales as $a_{SP} \simeq L S^{-1/2}$, and from conservation of mass the reconnection rate also scales as $S^{-1/2}$. Because the Lundquist number is typically very large in astrophysical systems (*e.g.* $S \sim 10^{12}$ – 10^{14} in solar corona), the Sweet-Parker reconnection rate is often too slow to account for observations. Furthermore, because the Sweet-Parker theory is inherently a steady-state theory, it also cannot explain the impulsive onset.

In recent years, significant progress has been made in understanding the fast reconnection rate. In particular, it is now well-established that the Sweet-Parker theory is not the correct description for resistive MHD reconnection in the high-Lundquist-number regime, because the reconnection layer is unstable to the plas-

moid instability (Biskamp 1993), which is a tearing-type instability (Furth et al. 1963). For two-dimensional (2D) reconnection, the elongated current sheet in the Sweet-Parker theory is replaced by a chain of plasmoids (or magnetic islands) and fragmented thin current sheets. In fully developed nonlinear stage, the reconnection rate becomes nearly independent of the Lundquist number (Lapenta 2008; Bhattacharjee et al. 2009; Cassak et al. 2009; Huang & Bhattacharjee 2010; Uzdensky et al. 2010; Loureiro et al. 2012; Ni et al. 2012; Huang & Bhattacharjee 2013; Takamoto 2013; Comisso et al. 2015; Loureiro & Uzdensky 2016). Furthermore, if the fragmented current sheets become thinner than kinetic scales such as ion inertial length d_i or ion gyro-radius ρ_i , even faster Hall/collisionless reconnection can be triggered (Daughton et al. 2009; Shepherd & Cassak 2010; Huang et al. 2011; Ji & Daughton 2011). In three dimensions (3D), the plasmoid instability can facilitate self-generated turbulent reconnection (Daughton et al. 2011; Oishi et al. 2015; Huang & Bhattacharjee 2016). Plasmoid-mediated reconnection has been studied in a wide range of contexts, including post-CME current sheets (Karpen et al. 2012; Guo et al. 2013; Lynch et al. 2016), weakly ionized plasmas (Leake et al. 2012, 2013), embedded reconnection in a broad outer current sheet (Cassak & Drake 2009), asymmetric reconnection (Murphy et al. 2013), relativistic reconnection (Takamoto 2013; Sironi et al. 2016), and statistical distribution of plasmoids (Fermo et al. 2010; Uzdensky et al. 2010; Loureiro et al. 2012; Huang & Bhattacharjee 2012).

Thus far, magnetic reconnection at the fully developed nonlinear stage of the plasmoid instability has been the focus of many studies. On the other hand, onset of fast reconnection facilitated by the plasmoid instability from the linear regime to nonlinear saturation remains not well-understood. The linear theory of plasmoid instability assuming a Sweet-Parker current sheet width $a_{SP} \simeq L S^{-1/2}$ gives a maximum growth rate γ_{max} satisfying the scaling relation $\gamma_{max} \tau_A \sim S^{1/4}$, where $\tau_A \equiv L/V_A$ is the Alfvénic time scale based on the current sheet length, and the corresponding wavenumber k_{max} of the fastest growing mode satisfies the scaling relation $k_{max} L \sim S^{3/8}$ (Tajima & Shibata 1997; Loureiro et al. 2007). These scaling relations indicate that a Sweet-Parker current sheet in high- S regime is drastically unstable and will generate an enormous number of plasmoids. However, because a Sweet-Parker sheet must be realized dynamically over time, the fact that γ_{max} diverges in the asymptotic limit $S \rightarrow \infty$ suggests that the current sheet will break apart before it reaches the Sweet-Parker width (Pucci & Velli 2014). This raises im-

portant questions about the condition for current sheet disruption: when does the current sheet break apart? what is the current sheet width when it does so? what is the dominant mode that disrupts the current sheet, and what is the corresponding growth rate? The answers to these questions have significant implications for the impulsive onset of fast magnetic reconnection.

The main objective of this paper is to investigate the plasmoid instability in dynamically evolving current sheets to address these questions, some of which are currently under debate in recent literature. Pucci & Velli (2014) argued that the maximum linear growth rate at disruption should become independent of S . From the scaling relations $\gamma_{max}\tau_A \sim S^{(3\alpha-1)/2}$ and $k_{max}L \sim S^{(5\alpha-1)/4}$ for a general situation where the current sheet width scales as $a \sim LS^{-\alpha}$ (Bhattacharjee et al. 2009; Pucci & Velli 2014), Pucci and Velli concluded that $\alpha = 1/3$ and proposed the inverse aspect ratio of the current sheet $a/L = S^{-1/3}$ as the condition for current sheet disruption; the corresponding maximum linear growth rate is a fixed value with $\gamma_{max}\tau_A = O(1)$ and the wavenumber satisfies the scaling relation $k_{max}L \sim S^{1/6}$. Two other recent theoretical studies by Uzdensky & Loureiro (2016) and Comisso et al. (2016) came to different conclusions regarding the disruption condition. Uzdensky & Loureiro (2016) assumed that the current sheet is essentially frozen when $\gamma\tau_{dr} = 1$, where τ_{dr} is the evolution time scale of the current sheet, and concluded that the fastest mode at that time will be the one that disrupts the current sheet. On the contrary, Comisso et al. (2016) found that the thinning process is important until the disruption time. Comisso et al. (2016) employed a principle of least time to derive analytically the scaling relations of the current sheet aspect ratio, the linear growth rate, and wavenumber of the dominant mode at disruption. These scaling relations are not power laws, with dependences not only on the Lundquist number S , but also on the noise level of the environment.

This work is distinct from previous studies in that we employ both direct numerical simulations and theoretical analysis of a phenomenological model. The corroboration between the two approaches puts our conclusions in solid footing. Our key findings can be summarized as follows:

1. The Sweet-Parker current sheet thickness a_{SP} can only be approached at low to moderately high Lundquist numbers. Therefore, there is a transition of scaling behavior from low- S to high- S regimes.

2. The current sheet disruption does not take place when $\gamma_{max}\tau_A = O(1)$, in contrast to the suggestion of Pucci & Velli (2014). In fact, the overall amplitude of fluctuation only starts to grow when $\gamma_{max}\tau_A = O(1)$, because the linear growth of tearing modes has to overcome the decrease of fluctuation amplitude due to advection loss and stretching effect of the outflow. Typically, the maximum linear growth rate satisfies $\gamma_{max}\tau_A \gg 1$ at disruption.
3. Contrary to what is commonly assumed, the dominant mode at disruption is not the fastest growing mode. Typically the dominant mode has a wavenumber approximately 3 to 6 times smaller than that of the fastest growing mode.
4. The dominant mode and growth rate at disruption cannot be determined by the Lundquist number S alone, as they also depend on the noise of the system.
5. The phenomenological model gives a prediction of the critical Lundquist number S_c for plasmoid instability, below which the instability cannot grow to a sufficient amplitude to disrupt the current sheet before it is advected out from the current sheet. Importantly, the critical Lundquist number S_c is not a fixed magnitude but depends weakly on the noise amplitude.

This paper is organized as follows. The details of the simulation setup are given in Section 2. Section 3 gives a description of our diagnostics for analyzing fluctuations in an evolving background and the condition for current sheet disruption. Section 4 presents the results from numerical simulations. In Section 5, we propose a phenomenological model that reproduces the scalings from simulation results and provides further insights. In Section 6, we discuss the transition from slow to fast reconnection after current sheet disruption and how the transition may be observed in solar spectroscopy through line profiles. We conclude and make comparisons with previous studies in Section 7.

2. SIMULATION SETUP

The governing equations for our simulations are non-dimensionalized two-dimensional (2D) resistive MHD equations:

$$\partial_t \rho + \nabla \cdot (\rho \mathbf{v}) = 0, \quad (1)$$

$$\partial_t (\rho \mathbf{v}) + \nabla \cdot (\rho \mathbf{v} \mathbf{v}) = -\nabla p - \nabla \psi \nabla^2 \psi + \nu \nabla^2 (\rho \mathbf{v}), \quad (2)$$

$$\partial_t \psi + \mathbf{v} \cdot \nabla \psi = \eta \nabla^2 \psi, \quad (3)$$

where standard notations are used. Here the Cartesian coordinate y is the direction of translational symmetry. The magnetic field \mathbf{B} is related to the flux function ψ via the relation $\mathbf{B} = \nabla \psi \times \hat{\mathbf{y}}$ and the electric current density $\mathbf{J} = -\nabla^2 \psi \hat{\mathbf{y}}$. An isothermal equation of state $p = 2\rho T$ with a constant temperature T is assumed. The numerical algorithm is detailed in (Guzdar et al. 1993), where derivatives are approximated by a five-point central finite difference scheme, with a fourth-order numerical dissipation equivalent to up-wind finite difference added to all equations for numerical stability. Time stepping is calculated by a trapezoidal leapfrog scheme. Explicit dissipations are employed through viscosity and resistivity.

We use the same simulation setup of two coalescing magnetic islands as in a previous study (Huang & Bhat-tacharjee 2010). The 2D simulation box is the domain $(x, z) \in [-1/2, 1/2] \times [-1/2, 1/2]$. In normalized units, the initial magnetic field is given by $\mathbf{B}_0 = \nabla \psi_0 \times \hat{\mathbf{y}}$, where $\psi_0 = \tanh(z/h) \cos(\pi x) \sin(2\pi z)/2\pi$. The parameter h , which is set to 0.01 for all simulations, determines the initial current layer width. The initial plasma density ρ is approximately unity, and the plasma temperature $T = 3$. The density profile has a weak nonuniformity such that the initial condition is approximately force-balanced. The initial peak magnetic field and Alfvén speed are both approximately unity. The plasma beta $\beta \equiv p/B^2 = 2\rho T/B^2$ is greater than 6 everywhere, hence the system is approximately incompressible. Perfectly conducting and free slipping boundary conditions are imposed along both x and z directions. Only the upper half of the domain ($z \geq 0$) is simulated, and solutions in the lower half are inferred by symmetries. We use a uniform grid of 37800 points along the x direction and a nonuniform grid of 2880 points along the z direction. The mesh along the z direction is packed to attain high resolution around $z = 0$, where the smallest grid size is 1.9×10^{-6} . The viscosity ν is set to 10^{-10} for all the simulations, and the resistivity η is varied from 2×10^{-6} to 2.5×10^{-8} , hence the magnetic Prandtl number $P_m \equiv \nu/\eta \ll 1$. The initial velocity is seeded with a random noise of amplitude ϵ to trigger the plasmoid instability. In these simulations, the current sheet half-length is approximately a constant value $L = 0.25$ and the upstream Alfvén speed is approximately $V_A = 1$. We use these values to define the Lundquist number $S = LV_A/\eta$ of the system. The simulation parameters and outcomes of diagnostics are summarized in Table 1.

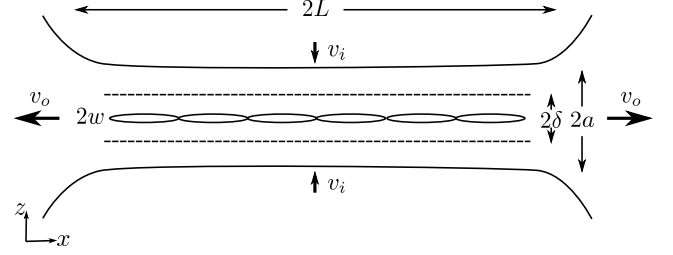


Figure 1. Schematic of plasmoid instability in a reconnecting current sheet. Here the length of the current sheet is $2L$, and the width is $2a$. Both the length and the width can be functions of time. The reconnection inflows and outflows are denoted as v_i and v_o , respectively. Within the current sheet are two additional length scales: the inner layer width 2δ , and the magnetic island width $2w$. The current sheet is disrupted when the magnetic island width exceeds the inner layer width.

3. DIAGNOSTICS

Before discussing the simulation results, we give the details of diagnostics employed in this study. Figure 1 shows a schematic of plasmoid instability in a reconnecting current sheet. Here the length of the current sheet is $2L$, and its width is $2a$. Both the length and the width can be functions of time. The reconnection inflows and outflows are denoted as v_i and v_o , respectively. There are two additional length scales within the current sheet: the inner layer width 2δ of the tearing mode, and the magnetic island width $2w$. We call the current sheet disrupted when the magnetic island width just exceeds the inner layer width, because at this time the fluctuating part of the current density is approximately of the same magnitude as the background.

In simulations, the inflows are along the z direction and the outflows are along the x direction. To measure the width of the current sheet, first we perform a tenth order polynomial fitting of J_y along the x direction between $x = -0.4$ to $x = 0.4$ for each z to smooth out fluctuations along x . Then we use the smoothed current density profile along the z direction at $x = 0$ to measure the current sheet width. In these simulations, we generally find that the current profile is reasonably well approximated by a Harris sheet with $J_y \propto \text{sech}^2(z/a)$. Therefore, in the following analysis and the rest of the paper a Harris sheet profile will be assumed. The half-width a is obtained by measuring the half-width at half-maximum (HWHM) and using the relation that the HWHM is $(\cosh^{-1} \sqrt{2})a \simeq 0.882a$ for a Harris sheet. Likewise, the half-length of the current sheet L is measured using the HWHM of the current density profile along the midplane $z = 0$. The measured length L is a non-monotonic function in time, and varies within the range 0.25 to 0.35 before disruption of the current sheet.

Run	S	ϵ	t_g	$\gamma_{max,g}$	a_g	t_d	a_d	δ_d	γ_d	γ_{max}	k_d	k_{max}	t_p	t_s
S1	1.25e5	10^{-6}	0.42	12.4	1.72e-3	1.24	7.47e-4	2.57e-4	14.6	43.1	81.4	414	1.81	2.01
S2	2.5e5	10^{-6}	0.42	9.61	1.60e-3	1.06	4.72e-4	1.69e-4	29.6	60.8	92.3	617	1.28	1.42
S3	5.0e5	10^{-6}	0.45	8.85	1.35e-3	1.00	3.37e-4	9.98e-5	44.5	71.3	157	791	1.13	1.25
S4	1.25e6	10^{-6}	0.52	9.74	9.35e-4	0.99	2.37e-4	5.90e-5	62.1	77.7	213	977	1.16	1.19
S5	2.5e6	10^{-6}	0.57	10.3	7.16e-4	1.00	1.83e-4	3.89e-5	69.7	79.4	282	1140	1.10	1.15
S6	5.0e6	10^{-6}	0.58	8.09	6.67e-4	1.02	1.40e-4	2.82e-5	74.0	83.9	287	1330	1.09	1.12
S7	1.0e7	10^{-6}	0.61	7.33	5.65e-4	1.04	1.09e-4	1.88e-5	77.3	86.7	374	1530	1.10	1.13
H1	1.25e5	10^{-3}	0.39	10.3	1.94e-3	0.87	6.77e-4	2.39e-4	26.2	50.0	92.3	468	1.17	1.18
H2	2.5e5	10^{-3}	0.43	10.3	1.55e-3	0.84	5.18e-4	1.51e-4	36.6	52.9	136	550	0.99	1.14
H3	5.0e5	10^{-3}	0.45	8.85	1.35e-3	0.84	3.99e-4	1.03e-4	43.1	53.5	169	640	0.96	1.04
H4	1.25e6	10^{-3}	0.52	9.74	9.35e-4	0.85	3.02e-4	6.66e-5	45.6	53.0	185	721	1.01	1.04
H5	2.5e6	10^{-3}	0.57	10.3	7.16e-4	0.88	2.33e-4	4.66e-5	47.5	55.4	209	839	1.01	1.05
H6	5.0e6	10^{-3}	0.58	8.09	6.67e-4	0.90	1.86e-4	3.01e-5	51.0	55.1	297	935	1.01	1.06
H7	1.0e7	10^{-3}	0.61	7.33	5.65e-4	0.93	1.64e-4	2.09e-5	52.9	56.6	346	920	1.02	1.06
N1	2.5e6	10^{-2}	0.57	10.3	7.16e-4	0.82	2.72e-4	4.87e-5	39.5	43.9	208	691	0.97	1.03
N2	2.5e6	10^{-5}	0.57	10.3	7.16e-4	0.96	1.97e-4	4.11e-5	64.3	71.1	256	1035	1.07	1.12
N3	2.5e6	10^{-9}	0.56	9.57	7.51e-4	1.09	1.61e-4	3.70e-5	83.0	96.0	292	1330	1.19	1.24

Table 1. Simulation parameters and outcomes from key diagnostics. The simulations are characterized by two input parameters: the Lundquist number S and the initial noise amplitude ϵ . The outcomes of diagnostics are listed as follows: t_g is the time when the overall fluctuation amplitude starts to grow; $\gamma_{max,g}$ is the maximum growth rate at $t = t_g$; a_g is the current sheet half-width at $t = t_g$; t_d is the disruption time; a_d is the current sheet half-width and δ_d is the inner layer half-width at disruption; γ_d is the measured growth rate and γ_{max} is the maximum growth rate at disruption; k_d is the dominant wavenumber and k_{max} is the fastest growing wavenumber at disruption; t_p is the time when the reconnection rate reaches the maximum; t_s is the nonlinear saturation time. These values are given in the normalized units employed in the simulations. In the normalized units, $V_A = 1$, $L = 0.25$, and $\tau_A = 0.25$.

As it is observed that the length L does not change substantially throughout the course of a simulation, we assume a fixed value $L = 0.25$ in the following discussion for simplicity. Another important quantity is the gradient of outflow velocity dv_x/dx , which determines the rate of mode-stretching along the x direction. We measure dv_x/dx at $x = 0$ by fitting a linear polynomial to the v_x profile along the midplane $z = 0$ between $x = -0.1$ to $x = 0.1$ and then taking the derivative.

To analyze the evolution of fluctuations due to the linear instability, fluctuations must be separated from the evolving background. Here we employ the B_z component of the magnetic field along the midplane $z = 0$ as the primary diagnostic. We identify the background by fitting B_z in $x \in [-L, L]$ as a superposition of Chebyshev polynomials $T_n(x/L)$ (see, *e.g.* Boyd (2001)), and the remaining part of B_z is the fluctuation \tilde{B}_z :

$$B_z(x) = \sum_{n=0}^m a_n T_n(x/L) + \tilde{B}_z(x), \quad (4)$$

where the coefficients a_n are determined by minimizing $\sum_{n=0}^m a_n^2$. Apparently, the resulting \tilde{B}_z from this separation depends on the order m of the polynomial expansion, especially during the early phase of the evolution when the amplitude of the fluctuation is much smaller than the amplitude of the background. Since the appropriate order m cannot be known *a priori*, we determine m adaptively by requiring that the amplitude of the fluctuation $\|\tilde{B}_z\| \equiv \left(\int_{-L}^L \tilde{B}_z^2 dx\right)^{1/2}$ is approximately stationary with respect to varying m . Specifically, the order m is determined by the following procedure. Starting from $m = 1$, we increase m by 2 in each step until the ratio $r_m \equiv \|\tilde{B}_z^m\|/\|\tilde{B}_z^{m-2}\|$ reaches a local maximum and $r_{m+2} \geq 0.95$. Here \tilde{B}_z^m denotes the fluctuation corresponding to a m -th order expansion, and we take odd values for m because $B_z(x)$ is approximately an odd function. The requirement $r_{m+2} \geq 0.95$ is set as a threshold to safeguard from rare cases when the amplitude of the fluctuation still decreases substantially with

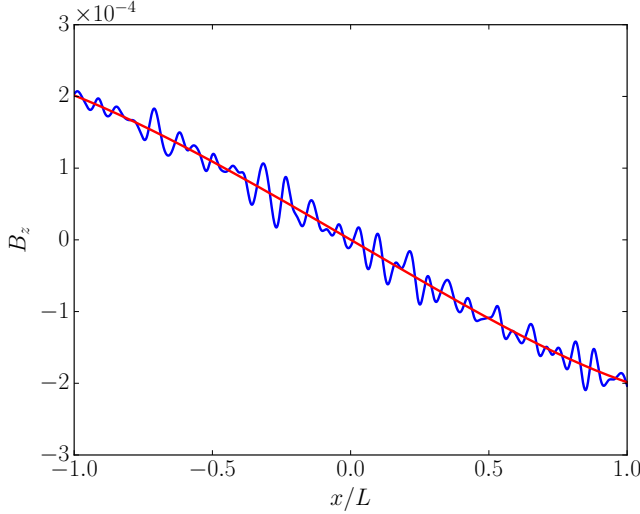


Figure 2. Separation of the fluctuation from the background. This example is taken from Run S5 at $t = 0.94$. The blue line is the total B_z along the midplane $z = 0$, and the red line is the polynomial fit (Eq. (4)) to determine the background. The order of Chebyshev polynomial expansion for the fitting, $m = 5$, is adaptively determined by the procedure outlined in the text. The difference between the total field B_z (blue line) and the smooth background (red line) is the fluctuation \tilde{B}_z .

increasing m immediately after reaching a local maximum of r_m . In most cases, typically $r_m > 0.99$ when these conditions are satisfied. An example illustrating the outcome from this procedure is shown in Fig. 2.

With the fluctuation \tilde{B}_z separated from the background, we can calculate the instantaneous growth rate as $\gamma = d \log \|\tilde{B}_z\| / dt$. We also obtain the Fourier spectrum of \tilde{B}_z to investigate the evolution of dominant wave number. Because \tilde{B}_z is not a periodic function, we multiply \tilde{B}_z by a C^∞ Planck-taper window function (McKechan et al. 2010), which equals unity within the range $-0.15 \leq x \leq 0.15$ and tapers off smoothly to zero over the ranges where $0.15 \leq |x| \leq 0.25$, before carrying out the Fourier transform. This step makes the “windowed” \tilde{B}_z vanish smoothly as x approaches $\pm L$, so that the Fourier spectrum will not be polluted by the mismatch between $\tilde{B}_z(L)$ and $\tilde{B}_z(-L)$. Hereafter, we denote the Fourier spectrum of the “windowed” \tilde{B}_z as $\tilde{B}_z(k)$, where k is the wavenumber. From the amplitude of the Fourier spectrum, we can identify the dominant wavenumber (more on this later). Note that the growth rate calculated here is the growth rate of the overall amplitude of the fluctuation rather than that of the dominant mode. However, because the Fourier spectrum is localized around the dominant wavenumber when the plasmoid instability is well-developed, the growth rate

calculated here also approximately represents that of the dominant mode.

The linear instability of tearing modes is governed by the tearing stability index Δ' (Furth et al. 1963), which is determined entirely by the solution of linearized ideal MHD force-free equation in the outer region away from the resonant surface, where $\mathbf{k} \cdot \mathbf{B} = 0$. The condition $\Delta' > 0$ must be satisfied for tearing instability. For a Harris sheet of half-width a , the tearing stability index Δ' for non-oblique tearing modes is given analytically as

$$\Delta' = \frac{2}{a} \left(\frac{1}{ka} - ka \right), \quad (5)$$

which gives the condition $ka < 1$ for instability. The dispersion relation for resistive tearing modes has been given in Coppi et al. (1976) and requires solving a transcendental equation. Analytical approximations can be obtained in two limits, the small- Δ' regime for short-wavelength modes, and the large- Δ' regime for long-wavelength modes. In the small- Δ' regime, the linear growth rate for a Harris sheet equilibrium is given by (Furth et al. 1963)

$$\gamma_s = C_\Gamma S_a^{-3/5} (ka)^{-2/5} (1 - k^2 a^2)^{4/5} \frac{V_A}{a}, \quad (6)$$

where $C_\Gamma = (\Gamma(1/4)/\pi\Gamma(3/4))^{4/5} \simeq 0.953$, and $S_a \equiv aV_A/\eta$ is the Lundquist number defined by the length scale a . In the large- Δ' regime, the linear growth rate is approximately given by (Coppi et al. 1976)

$$\gamma_l = S_a^{-1/3} (ka)^{2/3} \frac{V_A}{a}. \quad (7)$$

The fastest growing mode takes place at the transition between the two regimes, i.e. at $ka \sim S_a^{-1/4}$ when $\gamma_s \simeq \gamma_l$. More precisely, the fastest growing wavenumber k_{max} is given by (see, e.g. Schindler (2007))

$$k_{max} = \frac{1.358 S_a^{-1/4}}{a}, \quad (8)$$

and the corresponding growth rate is

$$\gamma_{max} = 0.623 S_a^{-1/2} \frac{V_A}{a}. \quad (9)$$

An approximate solution that captures the two asymptotic limits (6) and (7) is given by

$$\gamma = \frac{\gamma_s \gamma_l}{\left(\gamma_s^\zeta + \gamma_l^\zeta \right)^{1/\zeta}}, \quad (10)$$

for an arbitrary ζ . With some experimenting we find that the choice $\zeta = 3/2$ gives a nearly exact approximation to the true dispersion relation.

During the linear phase of the plasmoid instability, resistivity is important only within a narrow inner layer of thickness 2δ near the resonant surface, where (Biskamp 1993)

$$\delta = \left(\frac{\gamma}{V_A/a} \frac{1}{(ka)^2 S_a} \right)^{1/4} a. \quad (11)$$

The plasmoid instability enters the nonlinear regime when the magnetic island width $2w$ exceeds the inner layer width (Rutherford 1973). At this time, the electric current density fluctuation \tilde{J} is of the same order of the background current density, therefore the background current sheet loses its integrity and is “disrupted”. (The rationale for this description of a disrupted current sheet will become evident in Section 4.) For a single wavelength perturbation of the form $\tilde{B}_z = \tilde{B} \sin(kx + \phi)$, the island half-width is given by

$$w = 2\sqrt{\frac{\tilde{B}}{(ka)B_x}} a. \quad (12)$$

In real situations where the perturbation is a superposition of a spectrum of modes, one has to take a combination of neighboring modes (in the k space) of the dominant mode to estimate the island size. Here we consider a superposition over a range where k varies no more than a constant factor ξ , *i.e.* in the range $[k/\xi, k\xi]$. To identify the dominant wavenumber, we first smoothen the Fourier spectrum by a running average over $[k/\xi, k\xi]$ for each k . The dominant wavenumber is then determined by the peak of the smoothed spectrum. Once the dominant wavenumber k_d is determined, the combined contribution of neighboring modes in the range $[k_d/\xi, k_d\xi]$ to \tilde{B}_z can be estimated by the following relation

$$\begin{aligned} \frac{1}{\pi} \int_{k_d/\xi}^{k_d\xi} |\hat{B}_z(k')|^2 dk' &\simeq \int_{-L}^L |\tilde{B} \sin(k_d x)|^2 dx \\ &\simeq \tilde{B}^2 L, \end{aligned} \quad (13)$$

which gives

$$\tilde{B} = \left(\frac{1}{\pi L} \int_{k_d/\xi}^{k_d\xi} |\hat{B}_z(k')|^2 dk' \right)^{1/2}. \quad (14)$$

Using this relation for fluctuation amplitude \tilde{B} in Eq. (12), we can calculate the island half-width. The disruption time t_d is then determined as the moment when $w = \delta$ (in practice using the first snapshot with $w \geq \delta$), where the dominant wavenumber k_d is used to calculate δ in Eq. (11). Although the procedure outlined here depends on the constant factor ξ , as the spectrum $\hat{B}_z(k)$ is usually well-localized at the disruption time,

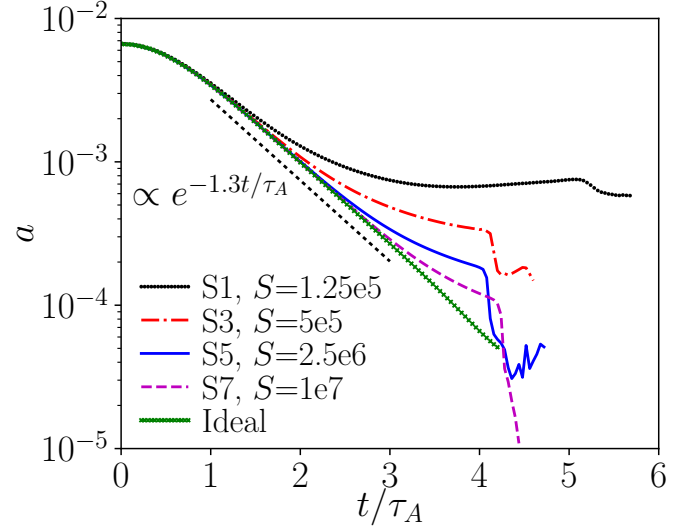


Figure 3. Time histories of the current sheet half-width a for selected cases. Also shown for reference is the time history from an ideal run, which exhibits a nearly perfect exponential thinning.

the result turns out to be insensitive to the choice of ξ , provided that ξ is not too close to unity. We choose the value $\xi = 1.5$ in this study.

4. SIMULATION RESULTS

The simulations all start with an initial current sheet half-width $a = 6.66 \times 10^{-3}$. As time progresses, the current sheet width decreases, as governed by the self-consistent resistive MHD equations. The time histories of $a(t)$ for selected runs with different Lundquist numbers S are shown in Fig. 3. It is observed that during the early period, the time history $a(t)$ is independent of S , indicating that the early phase of current sheet thinning is governed by ideal MHD. After a brief initial period, the current sheet width decreases exponentially in time according to the relation $a(t) \propto e^{-1.3t/\tau_A}$, until the resistive effect kicks in and slows down the thinning. When the plasmoid instability disrupts the current sheet, $a(t)$ appears to exhibit a sudden plummet, because the reconnection layer can no longer be identified as a single current sheet, and that makes the current sheet width diagnostic inapplicable. If the plasmoid instability does not disrupt the current sheet sufficiently rapidly, $a(t)$ will eventually approach the Sweet-Parker width as the asymptotic state. This is indeed the case for Run S1, where the Lundquist number is the lowest. For other cases with higher Lundquist numbers, the disruption takes place before the Sweet-Parker width is approached.

The diagnostics outlined in Sec. 3 are illustrated in Fig. 4 for Run S5. In panel (a) we show the time his-

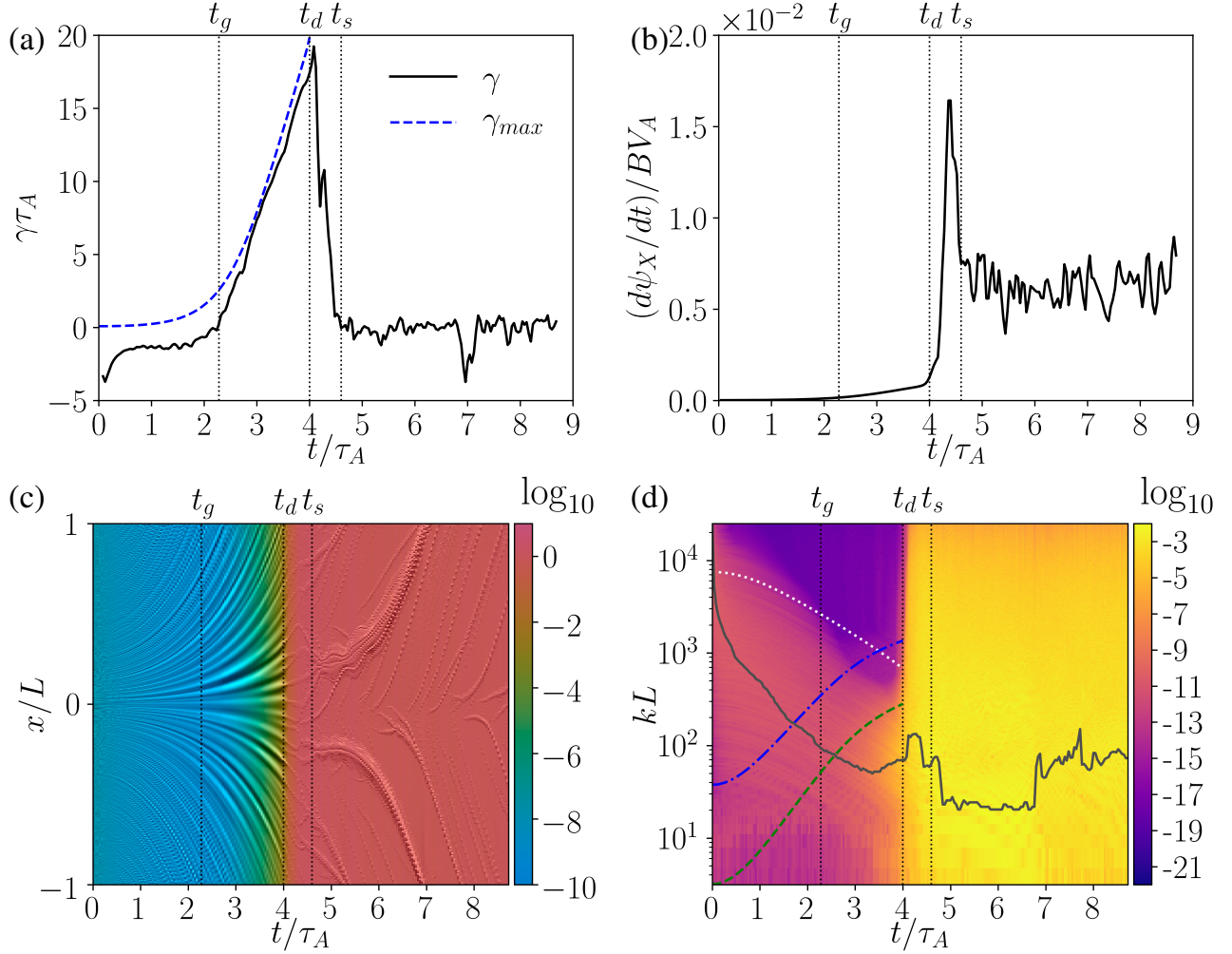


Figure 4. Diagnostics shown in time histories for Run S5. (a) The measured growth rate γ in solid line, and the maximum growth rate γ_{max} in dashed line. (b) Reconnection rate. (c) Fluctuation $\tilde{B}_z(x)$ in real space. Here hue is used to represent the maximum fluctuation amplitude $\max |\tilde{B}_z(x)|$ in logarithmic scale at each time, and luminance is used to indicate the relative amplitude (dark for negative and bright for positive). (d) Amplitude of the Fourier spectrum $|\hat{B}_z(k)|$ in logarithmic scale. The white dotted line indicates the trend of mode-stretching due to the outflow jets, *i.e.* $dk/dt = -kv'_x$; the blue dash-dot line denotes the stability threshold $ka = 1$; the green dashed line denotes the fastest growing wavenumber; the gray solid line denotes the dominant wavenumber. In all panels, t_g marks the time when the overall amplitude starts to grow, t_d marks the disruption time, and t_s marks the nonlinear saturation time.

tory of the growth rate γ and the maximum growth rate γ_{max} calculated with Eq. (9). Here (and in all other panels) we label three important times during the evolution: (1) The growth time t_g marks the time when γ goes from negative to positive, indicating the beginning of the growth of overall fluctuation amplitude. Here the measured growth rate is negative in the early period because of the advection loss and dissipation in the system. (2) The disruption time t_d marks the disruption time as identified by the condition $w = \delta$, and usually coincides well with the time when γ attains its maximum value and when $a(t)$ exhibits a sudden plummet. After $t = t_d$, the growth rate γ decreases rapidly. (3) The saturation time t_s marks the time beyond which γ

is approximately zero; *i.e.* the instability has reached nonlinear saturation. In panel (b) the time history of normalized reconnection rate is shown. Here the reconnection rate is measured by $d\psi_X/dt$, where ψ_X is the flux function ψ measured at the main X-point, where the two large-scale coalescing islands touch each other. The reconnection rate is normalized to BV_A , which equals unity in the normalized units. It can be seen that the reconnection rate increases rapidly after the disruption time t_d and reaches a maximum at a time (which is denoted as t_p in table 1) between t_d and the saturation time t_s then slows down. After the saturation time t_s , the reconnection rate essentially remains constant and fluctuates around an average value. In panel (c), the

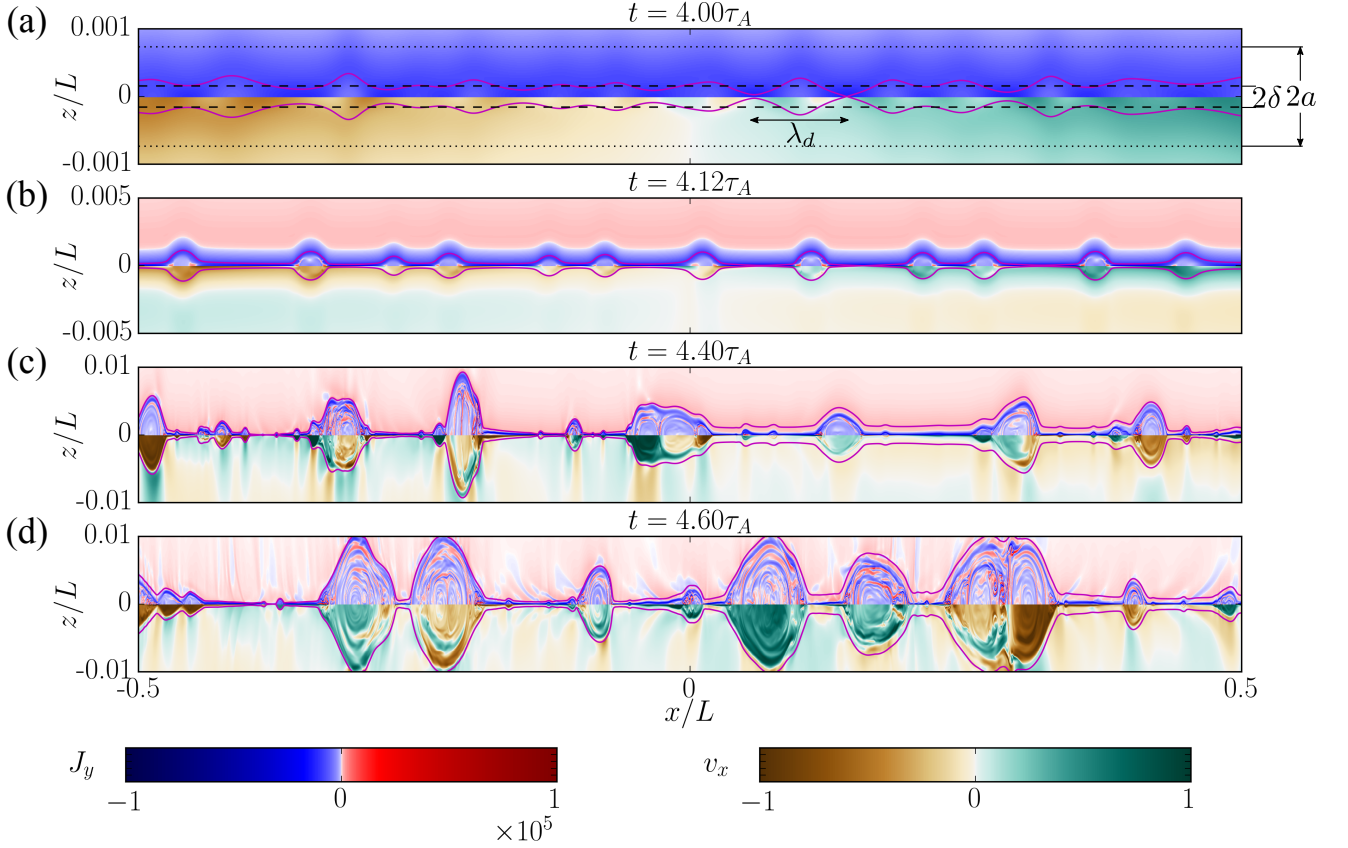


Figure 5. Representative snapshots between disruption and saturation for the Run S5. In each panel, the upper half shows the out-of-plane current density profile J_y and the bottom half shows the outflow profile v_x . The magenta solid lines denote the separatrices that separate the two large-scale coalescing islands. Note that the z direction is stretched in these plots, and the range along z direction varies from panel to panel to better show the plasmoids. Panel (a) shows a snapshot at the disruption time $t_d = 4\tau_A$. Here the dashed lines mark the inner layer width and the dotted lines mark the current sheet width at disruption. The dominant wavelength identified by our diagnostics, $\lambda_d = 2\pi/k_d$, faithfully represents the length scales of plasmoids along the x direction. Note that the x and z coordinates are normalized to the current sheet half-length L , as such the other length scales δ , a , and λ_d here are also normalized in the same manner. Panel (b) shows a snapshot after the disruption at $t = 4.12\tau_A$. At this time extended secondary current sheets have developed between plasmoids. These secondary current sheets are susceptible to the plasmoid instability and further fragmentation. This fractal-like cascade is clearly evident in Panel (c) at $t = 4.4\tau_A$, when the reconnection rate reaches the maximum. Panel (d) shows a snapshot when the plasmoid instability reaches nonlinear saturation.

fluctuation $\tilde{B}_z(x)$ in real space is shown. Here hue is used to represent the maximum fluctuation amplitude $\max|\tilde{B}_z(x)|$ at each time in logarithmic scale, and luminance is used to indicate the relative amplitude with respect to the overall amplitude (dark for negative and bright for positive). The effect of outflow jets in stretching the fluctuations is evident. Panel (d) shows the amplitude of Fourier spectrum $|\tilde{B}_z(k)|$ in logarithmic scale. This panel also shows several additional lines: the white dotted line indicates the trend of mode-stretching due to the outflow jets, *i.e.* $dk/dt = -kv'_x$; the blue dash-dot line denotes the stability threshold $ka = 1$; the green dashed line denotes the fastest growing wavenumber; the gray solid line denotes the dominant wavenumber. The Fourier spectrum amplitude is shown to follow the trend

$dk/dt = -kv'_x$ closely. Another noteworthy feature is that the dominant mode at disruption is not the fastest growing mode.

A sequence of representative snapshots from disruption to nonlinear saturation for Run S5 are shown in Fig. 5. In each panel, the upper half shows the out-of-plane current density profile J_y and the bottom half shows the outflow profile v_x . The magenta solid lines denote the separatrices that separate the two large-scale coalescing islands. Because the sizes of plasmoids evolve quite substantially during this period, the range along z direction varies from panel to panel to better accommodate the plasmoids at a given time. Panel (a) shows a snapshot at the disruption time $t_d = 4\tau_A$, when typical sizes of plasmoids just exceed the inner layer width.

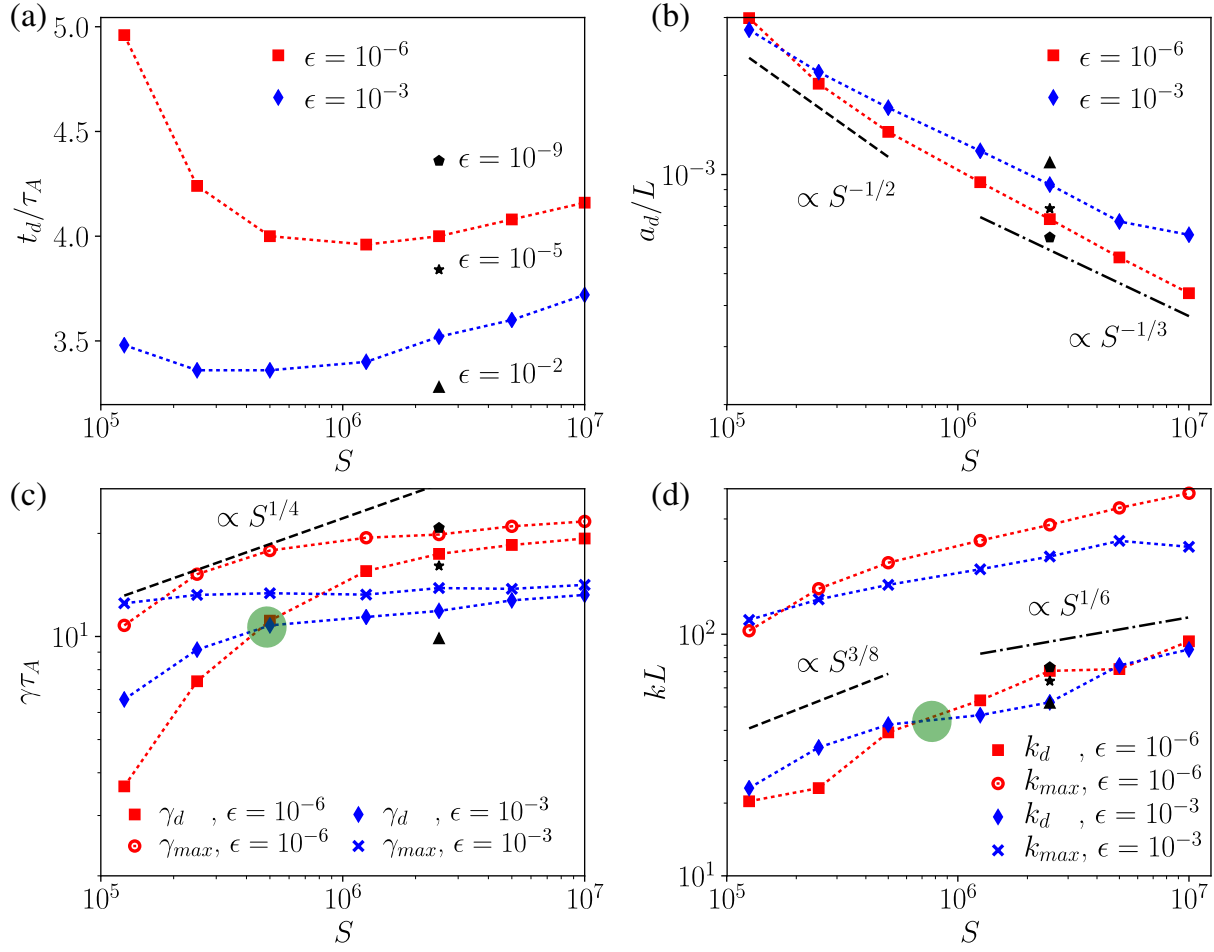


Figure 6. Scalings of the (a) disruption time t_d , (b) current sheet half-width a_d , (c) growth rate γ_d , and (d) dominant wavenumber k_d at disruption, with respect to S . Here red lines correspond to Runs S1–S7, with noise amplitude $\epsilon = 10^{-6}$, and blue lines correspond to Runs H1–H7, with noise amplitude $\epsilon = 10^{-3}$. Three black symbols in each panel represent Runs N1–N3 for different noise levels with $S = 2.5 \times 10^6$; see panel (a) for the legends. In panels (c) and (d), the growth rates and wavenumbers of the fastest mode (γ_{max} , k_{max}) and the dominant mode (γ_d , k_d) are both shown (only γ_d and k_d are shown for Runs N1–N3). The discrepancy between γ_{max} and γ_d are more pronounced at low S due to the effect of outflow. Note that the dominant wavenumber is significantly smaller than that of the fastest mode but they approximately follow the same trend. Green circles in panels (c) and (d) highlight the crossing between two $\gamma_d(S)$ curves and two $k_d(S)$ curves with different ϵ .

Here the dashed lines mark the inner layer width and the dotted lines mark the current sheet width at disruption. The dominant wavelength identified by our diagnostics, $\lambda_d = 2\pi/k_d$, is shown to faithfully represent the length scales of plasmoids along the x direction. In panel (b), a snapshot at $t = 4.12\tau_A$ shows that extended secondary current sheets have developed between plasmoids. These secondary current sheets are susceptible to the plasmoid instability and further fragmentation. This fractal-like cascade (Shibata & Tanuma 2001) is clearly evident in Panel (c) at $t = 4.4\tau_A$, when the reconnection rate reaches the maximum. Finally, panel (d) shows a snapshot when the plasmoid instability reaches nonlinear saturation.

Simulations of other cases all exhibit features qualitatively similar to those presented in Figs. 4 and 5. However, the quantitative values of diagnostic outcomes such as the disruption time t_d , current sheet half-width a_d , linear growth rate γ_d , and dominant wavenumber k_d depend on the parameters S and ϵ in a complex manner. The outcomes of diagnostics are summarized in Table 1, and plotted in Fig. 6 as scalings with respect to the Lundquist number S . The values in Table 1 are given in the original normalized units of the simulations. On the other hand, in Fig. 6, the quantities t_d , a_d , γ_d , and k_d are normalized to appropriate global scales τ_A and L ; recall that in the original normalized units, $V_A = 1$, $L = 0.25$, and $\tau_A = 0.25$. The panels in Fig. 6 are organized in two sets of parameter scans with respect

to S . Runs S1–S7 with noise amplitude $\epsilon = 10^{-6}$ are shown in red symbols, and runs H1–H7 with $\epsilon = 10^{-3}$ are shown in blue. Three additional runs N1–N3 with varying noise amplitudes at the same $S = 2.5 \times 10^6$ are shown in black symbols.

The growth time t_g marks the beginning when the overall amplitude starts to grow. It can be seen from Table 1 that the maximum growth rate $\gamma_{max,g} = O(10)$, *i.e.* $\gamma_{max,g}\tau_A \simeq 2-3$, at $t = t_g$ for all cases. This reaffirms the physical intuition that for the fluctuation amplitude to grow effectively, the growth rate has to be greater than the inverse of the time scale for current sheet evolution as well as that for the ejection of outflow jets, both of the order of τ_A . As will be made clear in Section 5, the overall amplitude of fluctuations can grow only when the linear growth from tearing modes is sufficient to overcome the decrease caused by advection loss and mode-stretching due to the outflow. Because at a higher S , the current sheet must thin down to a smaller width to achieve a maximum growth rate with $\gamma_{max,g}\tau_A \simeq 2-3$, it is observed that t_g increases monotonically with S . On the other hand, t_g is mostly independent of the initial noise amplitude ϵ , as long as the initial perturbation is sufficiently small to remain in the linear regime.

The disruption time t_d , shown in Fig. 6(a), is found to be non-monotonic with respect to S . This can be understood qualitatively as follows. At low Lundquist numbers, the current sheet width approaches the Sweet-Parker width before disruption. Since the plasmoid instability growth rate scales as $S^{1/4}$ for Sweet-Parker current sheets, it takes longer to disrupt a low- S current sheet because the growth rate is lower. On the other hand, at high Lundquist numbers, the current sheet will be disrupted before it approaches the Sweet-Parker width. However, the maximum growth rate has to reach $\gamma_{max}\tau_A = O(1)$ for the fluctuation to start growing, and it takes longer to reach that point at higher S . Consequently, the disruption time also becomes longer.

Figure 6(b) shows the scalings of current sheet half-width a_d at disruption. The scaling for cases with $\epsilon = 10^{-6}$ (red symbols) clearly shows a change in the scaling behavior as S increases. At low S , the scaling is close to $a_d \sim S^{-1/2}$, indicating that the current sheet is approaching the Sweet-Parker width at disruption. At high S , the scaling becomes less steep and is close to $a_d \propto S^{-1/3}$. For cases with $\epsilon = 10^{-3}$ (blue symbols), the scaling is close to $a_d \propto S^{-1/3}$ over the entire range of S we have scanned. Generally speaking, for fixed Lundquist number, the time to disruption is longer when the initial noise is smaller, and therefore, a_d is smaller. This trend is evident for the runs

S5, H5, and N1–N3 with $S = 2.5 \times 10^6$. However, we note an exception to this rule for runs S1 and H1, both at $S = 1.25 \times 10^5$, where a_d is found to be larger for run S1, even though the initial noise is smaller. This happens because $a(t)$ is not necessarily a monotonically decreasing function. It is well-known that the two large-scale merging islands can bounce back, in a phenomenon known as “sloshing”, after the distance between them reaches a minimum (Knoll & Chacón 2006). When the two islands bounce back, the current sheet half-width $a(t)$ increases. It can be seen from Fig. 3 that disruption occurs when $a(t)$ is weakly increasing for run S1, therefore a_d for run S1 is larger than that for run H1, in which disruption occurs at an earlier time. Note that sloshing takes place before disruption only at low S , because at high S , disruption usually takes place before the distance between the two large-scale islands reaches a minimum.

The scalings of the linear growth rate at disruption are shown in Fig. 6(c). Here the scalings for two growth rates are shown: the growth rate γ_d measured from simulations, and the fastest growth rate γ_{max} calculated from Eq. (9) with $a = a_d$. The measured growth rate γ_d is smaller than the maximum growth rate γ_{max} , which is understandable as the dominant mode is not the fastest growing mode. The discrepancy between γ_d and γ_{max} is more pronounced at lower S , because mode-stretching due to outflow jets becomes more effective (more on this in Sec. 5). For cases with $\epsilon = 10^{-6}$, the maximum growth rate $\gamma_{max} \sim S^{1/4}$ at lower S and becomes nearly independent of S at higher S ; for cases with $\epsilon = 10^{-3}$, γ_{max} is approximately independent of S in the range we have scanned. These scalings are direct consequences of the scalings of a_d we discussed previously. Likewise, the scalings of the dominant wavenumber k_d and the fastest growing wavenumber k_{max} at disruption are shown in Fig. 6(d). Here, the dominant wavenumber k_d is observed to be smaller than the fastest growing wavenumber k_{max} by a factor of approximately 3 to 6, where the factor tends to be larger at lower S . Because the spectrum $\hat{B}_z(k)$ at disruption is not a very sharp peak, there is considerable uncertainty in determining the dominant wavenumber, and this is reflected in the irregular appearance of the scalings of k_d . We should point out that the various power-law scalings shown in Fig. 6 (b)–(d) are only for reference; they should not be interpreted as the actual scalings of those quantities.

A notable feature in Fig. 6(c) is the crossing, highlighted by the green circle, between the two $\gamma_d(S)$ curves for different initial noise amplitudes. Generally speaking, if the noise amplitude is lower, it takes longer to disrupt the current sheet, hence the current sheet is thin-

ner at disruption and the growth rate is higher. This trend is observed at high S but the trend is the opposite at low S , leading to the crossing of the two $\gamma_d(S)$ curves. A similar crossing is also observed for the two $k_d(S)$ curves in Fig. 6(d), although it is less clean due to the greater uncertainty in obtaining k_d . As will be discussed in greater detail in Sec. 5, this “crossing” between S -dependence curves is due to the stretching effect of the outflow, which causes a significant departure of the dominant mode from the fastest growing mode at low S . Ultimately, this crossing is linked to the notion of the “critical” Lundquist number S_c for the plasmoid instability, which turns out to depend on the initial noise amplitude instead of being a constant value.

5. PHENOMENOLOGICAL MODEL FOR CURRENT SHEET DISRUPTION

The simulation results presented in Sec. 4 regarding the scalings of various quantities at disruption can be reproduced, at least qualitatively, with a simple model. In this model, we seek a description for the time evolution of fluctuation in the Fourier space, in terms of a normalized amplitude $f(k, t) \equiv |\tilde{B}_z(k, t)|/B_0 L_0$, where B_0 is a characteristic magnetic field and L_0 is a characteristic length. In this model, we allow the current sheet length and width to evolve in time.

Assuming that the outflow velocity v_x profile is approximately linear, the mode-stretching due to outflow implies that $f(k, t)$ will be advected in k -space following the time evolution of wavenumber k :

$$\frac{dk}{dt} = -v'_x k, \quad (15)$$

where $v'_x = dv_x/dx$ is the gradient of the outflow velocity. However, the fluctuation amplitude $f(k, t)$ can also change when it is advected, as will be determined as follows.

Taking the z component of the linearized ideal induction equation along the mid-plane $z = 0$ yields

$$\partial_t \tilde{B}_z + v_x \tilde{B}'_z = -\tilde{B}_z v'_x. \quad (16)$$

Here the left-hand-side of Eq. (16) represents the rate of change of \tilde{B}_z in the reference frame moving with the plasma, which is equal to the right-hand-side representing the change of \tilde{B}_z due to stretching or compression. Because we are interested in fluctuations within the current sheet, we seek the time dependence of the L^2 -norm of \tilde{B}_z over the current sheet region $||\tilde{B}_z||^2 \equiv \int_{-L}^L \tilde{B}_z^2 dx$. First, we multiply Eq. (16) by \tilde{B}_z and integrate from $x = -L$ to L to yield (after integrating by parts and multiplying by a factor of two)

$$\int_{-L}^L \partial_t \tilde{B}_z^2 dx = -v_x \tilde{B}_z^2|_{-L}^L - v'_x \int_{-L}^L \tilde{B}_z^2 dx, \quad (17)$$

where the first term on the right hand side accounts for the advection loss, and the second term is the contribution from stretching. To evaluate the first term we need v_x and \tilde{B}_z^2 at the end points $x = \pm L$. The outflow velocity $v_x = \pm v_o$ at $x = \pm L$, but \tilde{B}_z^2 at end points fluctuate in time and cannot be known beforehand. To proceed, we further assume that the amplitude of \tilde{B}_z is approximately uniform along the current sheet, and replace \tilde{B}_z^2 at $x = \pm L$ with the averaged value $\frac{1}{2L} \int_{-L}^L \tilde{B}_z^2 dx$ over the entire current sheet length. This approximation is valid if the time scale of interest (*i.e.* the time scale on which $||\tilde{B}_z||^2$ evolves) is longer than the typical fluctuating time scale of \tilde{B}_z at the end points, which is justified according to our simulations (see Fig. 4(c)). Under this assumption, we obtain the advection loss term $v_x \tilde{B}_z^2|_{-L}^L \simeq \frac{v_o}{L} \int_{-L}^L \tilde{B}_z^2 dx = v'_x \int_{-L}^L \tilde{B}_z^2 dx$, which is the same as the contribution from stretching. Hence, Eq. (17) can be written as

$$\int_{-L}^L \partial_t \tilde{B}_z^2 dx = -2v'_x \int_{-L}^L \tilde{B}_z^2 dx. \quad (18)$$

Taking into account that the current sheet length L can evolve in time and applying Leibniz's rule, we obtain the time rate of change of the L^2 -norm of \tilde{B}_z over the current sheet region

$$\begin{aligned} \frac{d}{dt} \int_{-L}^L \tilde{B}_z^2 dx &= \int_{-L}^L \partial_t \tilde{B}_z^2 dx + \frac{dL}{dt} \left(\tilde{B}_z^2|_{x=L} + \tilde{B}_z^2|_{x=-L} \right) \\ &= \left(-2v'_x + \frac{1}{L} \frac{dL}{dt} \right) \int_{-L}^L \tilde{B}_z^2 dx. \end{aligned} \quad (19)$$

Here, in the second step we apply Eq. (18) for the first term on the right hand side, and again approximate \tilde{B}_z^2 at $x = \pm L$ with the averaged value $\frac{1}{2L} \int_{-L}^L \tilde{B}_z^2 dx$. Equation (19) accounts for the change of the L^2 -norm due to the combined effects of stretching, advection loss, and evolution of the current sheet length, where the former two effects give the same contribution (hence the factor of two in the v'_x term). For the special case that the current sheet is lengthening with the same speed as the outflow, *i.e.* $dL/dt = v_o$, the latter two effects exactly cancel each other because the outflow cannot escape from the current sheet, therefore only the contribution from stretching effect remains.

The next step is to rewrite the L^2 -norm of \tilde{B}_z in Fourier space using the relation $\int_0^\infty |\hat{B}_z|^2 dk = \pi \int_{-L}^L |\tilde{B}_z|^2 dx$ in Eq. (19). The time derivative of

$\int_0^\infty |\hat{B}_z|^2 dk$ can be expressed as

$$\begin{aligned} \frac{d}{dt} \int_0^\infty |\hat{B}_z|^2 dk &= \int_0^\infty \frac{d}{dt} (|\hat{B}_z|^2 dk) \\ &= \int_0^\infty \frac{d|\hat{B}_z|^2}{dt} dk + \int_0^\infty |\hat{B}_z|^2 \frac{d}{dt} dk \\ &= \int_0^\infty \frac{d|\hat{B}_z|^2}{dt} dk - \int_0^\infty |\hat{B}_z|^2 v'_x dk, \end{aligned} \quad (20)$$

where the time derivative d/dt on the right hand side is the Lagrangian time derivative in Fourier space following the stretching of wavenumber k in Eq. (15), *i.e.*

$$\frac{d}{dt} = \frac{\partial}{\partial t} + \frac{dk}{dt} \frac{\partial}{\partial k} = \frac{\partial}{\partial t} - kv'_x \frac{\partial}{\partial k}. \quad (21)$$

Note that because the wavenumber k evolves in time from the Lagrangian viewpoint, the differential wavenumber dk also evolves according to the relation $d(dk)/dt = -v'_x dk$. Alternatively, Eq. (20) can be derived from the Eulerian viewpoint and applying Eq. (21):

$$\begin{aligned} \frac{d}{dt} \int_0^\infty |\hat{B}_z|^2 dk &= \int_0^\infty \frac{\partial}{\partial t} |\hat{B}_z|^2 dk \\ &= \int_0^\infty \frac{d}{dt} |\hat{B}_z|^2 dk + \int_0^\infty kv'_x \frac{\partial}{\partial k} |\hat{B}_z|^2 dk \\ &= \int_0^\infty \frac{d}{dt} |\hat{B}_z|^2 dk - \int_0^\infty |\hat{B}_z|^2 v'_x dk \\ &\quad + kv'_x |\hat{B}_z|^2 \Big|_{k=0}^{k=\infty}. \end{aligned} \quad (22)$$

Assuming that $|\hat{B}_z|^2$ vanishes at $k = 0$ and ∞ , we obtain the same relation as Eq. (20).

Using Eq. (20) in Eq. (19) yields

$$\int_0^\infty \frac{d|\hat{B}_z|^2}{dt} dk = \left(-v'_x + \frac{1}{L} \frac{dL}{dt} \right) \int_0^\infty |\hat{B}_z|^2 dk. \quad (23)$$

Here the right hand side represents the effects of advection loss and evolution of the current sheet length, while the stretching effect is incorporated in the Lagrangian time derivative on the left hand side. From Eq. (23), we obtain the Lagrangian time derivative of the Fourier component amplitude:¹

$$\frac{d|\hat{B}_z|}{dt} = \left(-\frac{v'_x}{2} + \frac{1}{2L} \frac{dL}{dt} \right) |\hat{B}_z|. \quad (24)$$

¹ The reader may wonder how the Fourier amplitude can change due to change in L . The reason is that we are considering fluctuations within the current sheet, from $x = -L$ to $x = L$, and project that onto the Fourier components. Hence the projection becomes larger (smaller) when L increases (decreases).

As a consistency check, note that this equation also gives the correct physical condition that magnetic island width does not change due to stretching, as can be verified by taking the time derivative of the island half-width w from Eq. (12), applying Eq. (14) and Eq. (24).

The model is completed by adding the contribution from the linear growth of tearing instability $\gamma |\hat{B}_z|$ to the right hand side of Eq. (24), which gives the time evolution equation for the fluctuation amplitude $|\hat{B}_z|$ in Fourier space. The final model equation is expressed in terms of the normalized fluctuation amplitude, $f(k, t) \equiv |\hat{B}_z(k, t)|/B_0 L_0$, as:

$$\frac{df}{dt} = \partial_t f - kv'_x \partial_k f = \left(\gamma - \frac{v'_x}{2} + \frac{1}{2L} \frac{dL}{dt} \right) f. \quad (25)$$

Here, the growth rate γ depends on time through the time dependence of the current sheet half-width $a(t)$ and the upstream magnetic field $B(t)$. We further limit the domain to the region $k \geq k_{min} \equiv \pi/L$, below which the wavelength cannot be contained in the current sheet. If we take the Lagrangian viewpoint of following the stretching of a mode according to Eq. (15), the wavelength of the mode becomes longer over time. At a certain point, the wavelength will be stretched to become longer than the length of the current sheet, and we can say that the mode is advected out of the current sheet.

It can be shown from Eq. (25) that the time rate of change of the L^2 -norm of the fluctuation, limited to the domain $k \geq k_{min}$, is given by

$$\begin{aligned} \frac{d}{dt} \int_{k_{min}}^\infty f^2 dk &= \int_{k_{min}}^\infty 2\gamma f^2 dk - v'_x \int_{k_{min}}^\infty f^2 dk \\ &\quad + \left(\frac{1}{L} \frac{dL}{dt} - v'_x \right) \left(kf^2 \Big|_{k_{min}} + \int_{k_{min}}^\infty f^2 dk \right). \end{aligned} \quad (26)$$

The first term on the right hand side of Eq. (26) accounts for the increase in fluctuation amplitude due to tearing modes. The second term is the decrease due to stretching effect. The third term accounts for the effects of advection loss and the evolution of current sheet length, where the surface term $kf^2|_{k_{min}}$ comes from integration by parts and application of Leibniz's rule on the lower bound k_{min} of the integral (note that $dk_{min}/dt = -(k_{min}/L)dL/dt$.) The effects of advection loss and the evolution of current sheet length exactly cancel each other when the current sheet is lengthening with the outflow speed, *i.e.* $dL/dt = v_o$, as the outflow cannot escape from the current sheet. However, in general we should expect $dL/dt \leq v_o$, hence the third term on the right hand side of Eq. (26) is also negative. As such, to have a positive growth of the L^2 -norm, the linear growth rate of tearing mode has to be sufficiently

large to overcome the decrease due to advection loss and stretching. Under most circumstances, the surface term $k f^2|_{k_{min}}$ is negligible compared to $\int_{k_{min}}^{\infty} f^2 dk$, as long as the dominant wavenumber is much larger than k_{min} . If we further assume that $|dL/dt| \ll v_o$, then

$$\frac{d}{dt} \int_{k_{min}}^{\infty} f^2 dk \simeq \int_{k_{min}}^{\infty} 2(\gamma - 1/\tau_A) f^2 dk. \quad (27)$$

Since γ is a function of k , Eq. (27) gives $\gamma_{max}\tau_A > 1$ as a minimum requirement for a positive growth of the overall fluctuation amplitude, which is consistent with our simulation findings.

Equation (26) implies that if the plasmoid instability does not exist, the fluctuation amplitude will decrease monotonically in time and asymptotically approach zero as $t \rightarrow \infty$. However, since noise is always present in any natural systems, noise will replenish the fluctuation and prevent it from approaching zero even in the absence of the plasmoid instability. Noise can be introduced into the model by explicitly adding a source term or by setting a floor to the fluctuation amplitude as a lower bound. To properly model noise in the system requires extra knowledge of the environment, and will not be discussed further here. For the cases we consider here, the plasmoid instability sets in sufficiently rapidly and the decay of fluctuation amplitude is not a significant issue.

Up to this point, the time dependences of the current sheet half-width a , the half-length L , the upstream magnetic field B , and the velocity gradient v'_x are not specified. These conditions must be provided according to the physical system under consideration. To fix the idea, we consider a situation when L and B are no longer evolving, *i.e.* $L = L_0$ and $B = B_0$. Let v_i and v_o be the inflow and the outflow speeds, respectively. Assuming an incompressible plasma, conservation of mass and energy implies that $v_o = B_0/\sqrt{\rho} = V_A$ and $v_i = aV_A/L_0$, as in the Sweet-Parker model. Therefore, the velocity gradient $v'_x = V_A/L = 1/\tau_A$ is independent of time. The time-dependence of the half-width $a(t)$ can be obtained by integrating the induction equation $\partial_t \mathbf{B} = -\nabla \times \mathbf{E}$ from $z = 0$ to the asymptotic outer region $z = z_{out} \gg a$, which yields

$$\frac{d}{dt} \int_0^{z_{out}} B_x dz = E_y|_{z_{out}} - E_y|_0. \quad (28)$$

Assuming a Harris sheet profile $B_x = B_0 \tanh(z/a)$ and formally setting $z_{out} \rightarrow \infty$, using the relations $E_y|_{\infty} = v_i B_0 = aV_A B_0/L_0$ and $E_y|_0 = \eta J_y|_{z=0} = \eta B_0/a$, we obtain

$$\frac{d}{dt} \int_0^{\infty} B_0 \tanh(z/a) dz = \frac{aV_A}{L} B_0 - \eta \frac{B_0}{a}. \quad (29)$$

The left-hand-side can be calculated using

$$\begin{aligned} \frac{d}{dt} \int_0^{\infty} \tanh(z/a) dz &= -\frac{da}{dt} \int_0^{\infty} \frac{z}{a^2} \text{sech}^2(z/a) dz \\ &= -\log(2) \frac{da}{dt}, \end{aligned} \quad (30)$$

hence we obtain a time evolution equation for $a(t)$:

$$\log(2) \frac{da}{dt} + \frac{V_A}{L} a - \frac{\eta}{a} = 0. \quad (31)$$

The solution is

$$a^2 = a_{SP}^2 + (a_0^2 - a_{SP}^2) \exp(-(2/\log 2)(t/\tau_A)), \quad (32)$$

where a_0 is the half-width at $t = 0$ and $a_{SP} = L/\sqrt{S}$ is the Sweet-Parker width.² This solution approaches a_{SP} in the asymptotic limit $t \rightarrow \infty$. At high S with $a_{SP} \ll a_0$, the half-width decays exponentially with $a \simeq a_0 \exp(-1.44 t/\tau_A)$ at early time. This is in good agreement with what we obtain in simulations, shown in Fig. 3, apart from an initial transient period before the Alfvénic outflow jets have been established.

To apply the model equation, an initial condition must be prescribed for the fluctuation amplitude $f(k)$. For the time evolution of a current sheet given in the previous paragraph, we can solve Eq. (25) using the method of characteristics. Along a characteristic following the stretching of wavenumber

$$k = k_0 e^{-t/\tau_A}, \quad (33)$$

the solution is

$$f(k, t) = f_0(k_0) \exp\left(\int_0^t \gamma(k(t'), a(t')) dt' - \frac{t}{2\tau_A}\right), \quad (34)$$

where $f_0(k)$ is the initial condition. We numerically integrate Eq. (34) to obtain the solution. To fix the idea, we set the initial half-width $a_0 = L/\pi$ such that the longest mode allowed in the model with $k = k_{min}$ is marginally unstable. We identify the dominant wavenumber by the peak of $f(k)$ and determine the disruption time by the criterion that the island size equals the inner layer width, using the same procedure outlined in Sec. 3 to calculate the island width.

We first assume the initial condition to be a constant value, $f_0(k) = \epsilon$.³ As an example, the solution for

² An alternative derivation of a similar functional form can be found in Kulsrud (2005), page 425 – 426.

³ Strictly speaking, a constant $f_0(k) = \epsilon$ is not permitted, because $\int_{k_{min}}^{\infty} f_0^2 dk$ diverges. This problem can be overcome if we assume that $f_0(k) = \epsilon$ for a broad range of k but approaches zero for very high- k modes. As long as those high- k modes never become unstable to the tearing instability (following mode-stretching), the results we obtain remain unchanged.

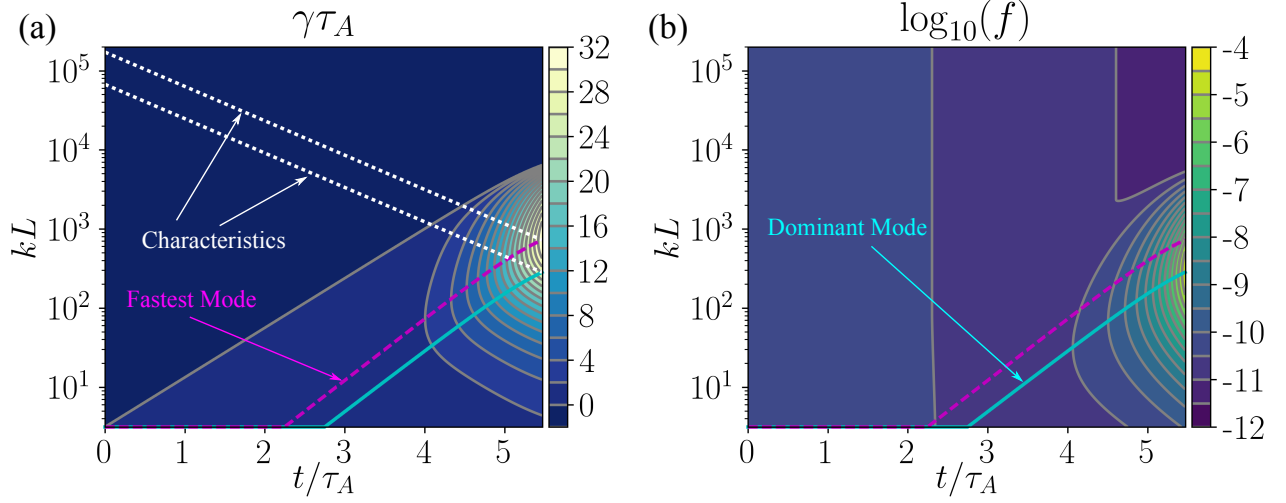


Figure 7. (a) Linear growth rate, and (b) solution of the model equation (25) for the case $S = 10^8$, $\epsilon = 10^{-10}$. Also marked in the panels are the wavenumbers for the fastest growing mode (magenta dashed line) and the dominant mode (cyan solid line). The white dotted lines in panel (a) are characteristics corresponding to the dominant mode and the fastest mode at disruption.

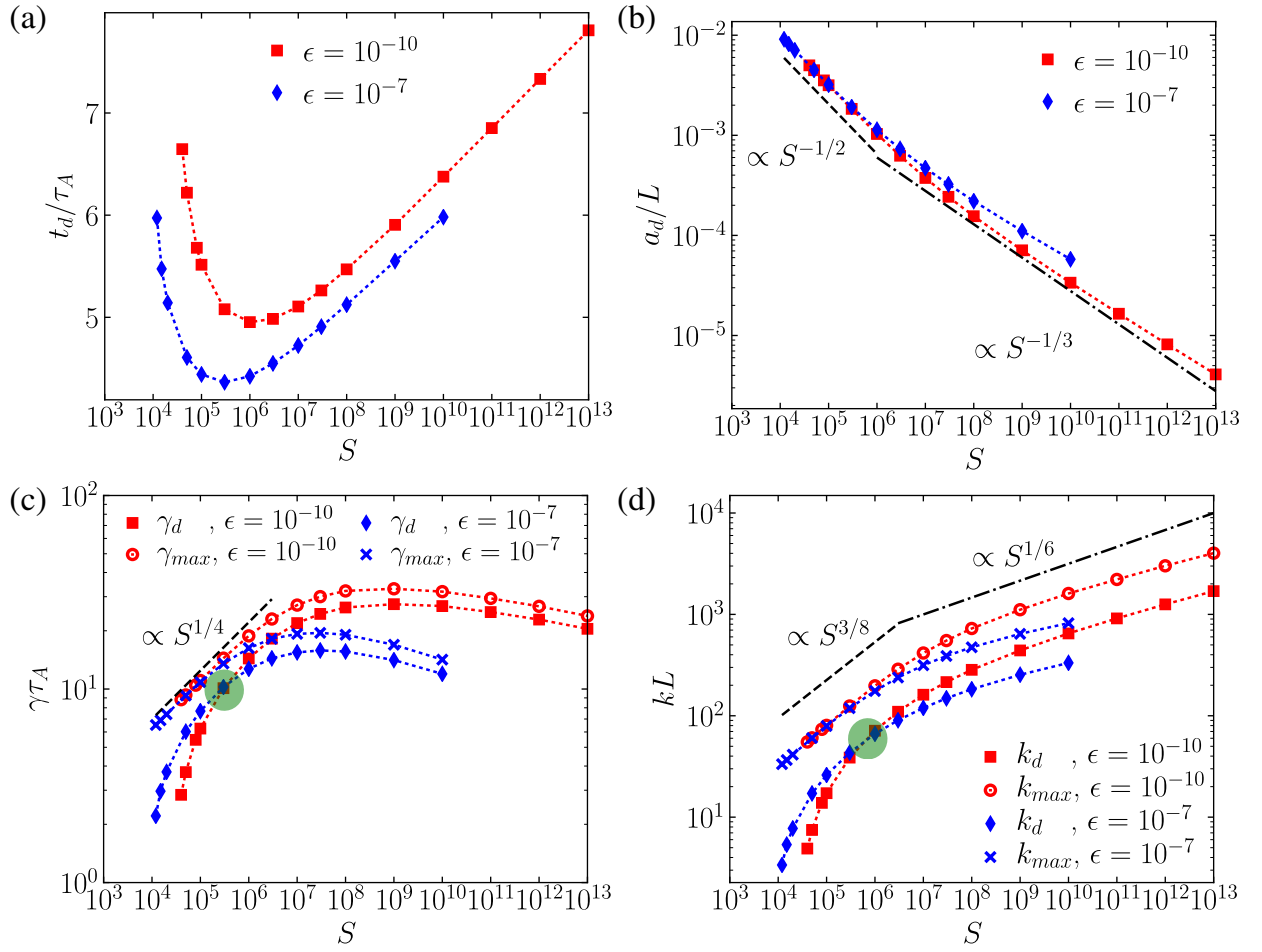


Figure 8. Scalings of t_d , a_d , k_d , and γ_d with respect to S from the model with $f_0(k) = \epsilon$, for $\epsilon = 10^{-7}$ and 10^{-10} . Green circles in panels (c) and (d) highlight the crossing between two $\gamma_d(S)$ curves and two $k_d(S)$ curves with different ϵ .

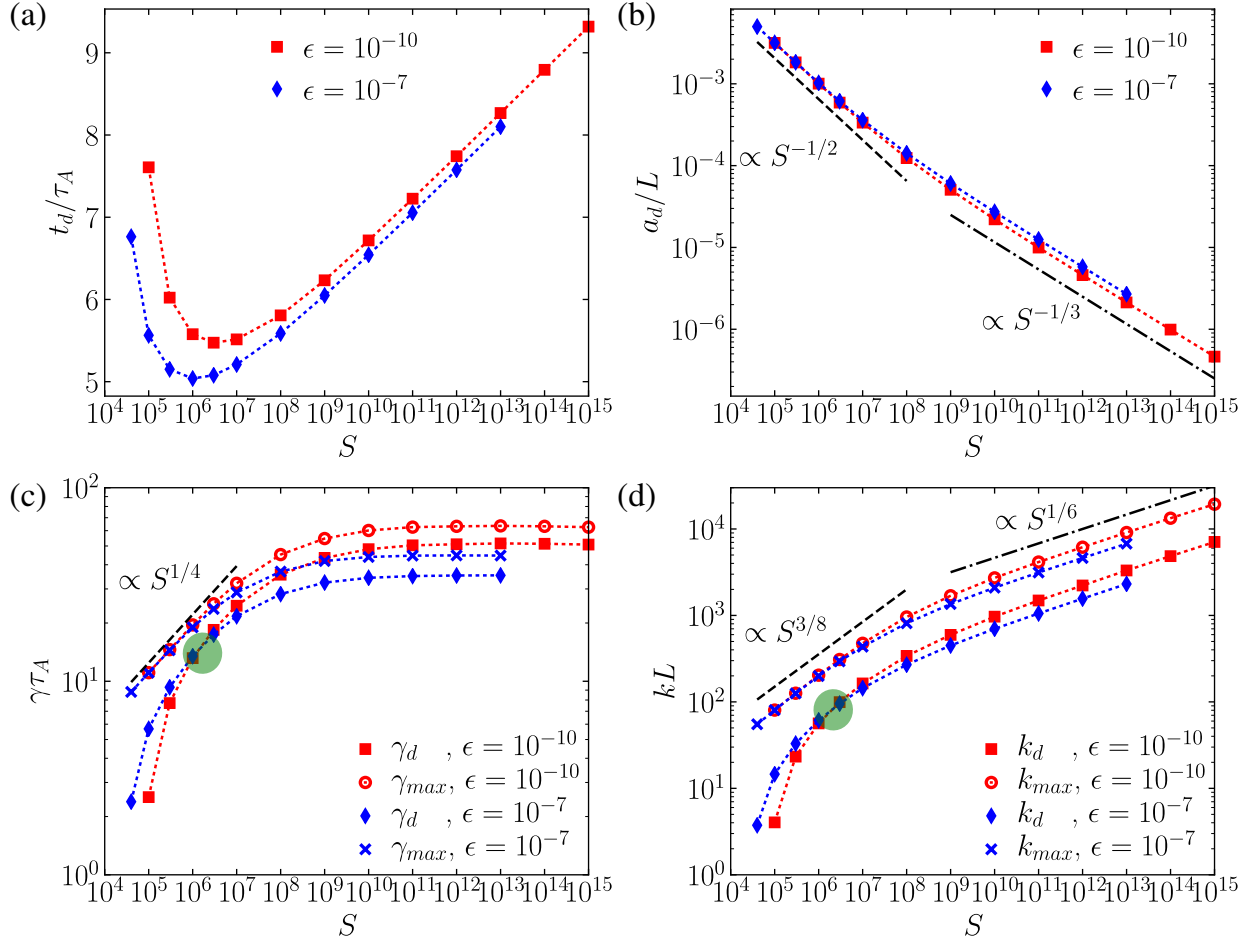


Figure 9. Scalings of t_d , a_d , k_d , and γ_d with respect to S from the model, with an initial noise $f_0 = \epsilon(k/k_{min})^{-1}$, for $\epsilon = 10^{-7}$ and 10^{-10} . Green circles in panels (c) and (d) highlight the crossing between two $\gamma_d(S)$ curves and two $k_d(S)$ curves with different ϵ .

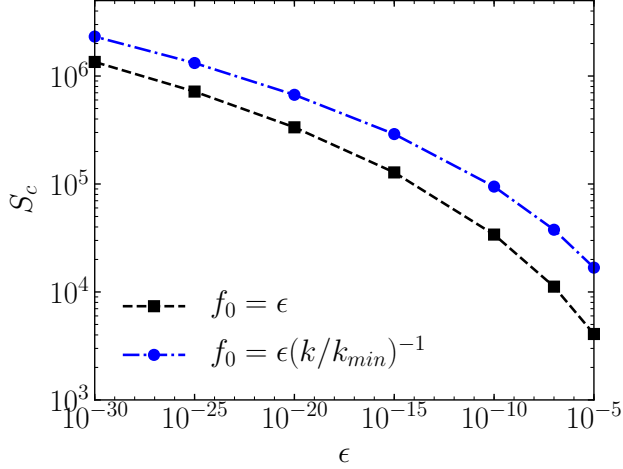


Figure 10. Critical Lundquist number S_c as a function of initial noise, for $f_0(k) = \epsilon$ and $f_0(k) = \epsilon(k/k_{min})^{-1}$.

the case $S = 10^8$ and $\epsilon = 10^{-10}$ is shown in Figure 7. Here panel (a) shows the linear growth rate as a function of time and k , and panel (b) shows the solution obtained from integrating Eq. (34). The time integration concludes when the disruption condition is met. Also shown in these panels are the wavenumber of the fastest growing mode and that of the dominant mode at each instant of time. The wavenumber of the dominant mode is found to be smaller than that of the fastest growing mode, which is consistent with the simulation results. The reason that the dominant mode does not coincide with the fastest growing mode at disruption can be seen from their corresponding characteristics, shown as white dotted lines in panel (a). Because the exponent in Eq. (34) is given by the integration of the linear growth rate over the characteristic, the amplification of a mode is determined by the entire history. As can be seen from Fig. 7(a), although the fastest growing mode has a higher growth rate at the final moment before disruption, the dominant mode actually becomes unstable earlier and grows faster during most of the time.

The scalings of t_d , a_d , γ_d , and k_d from the model are shown in Figure 8 for $\epsilon = 10^{-7}$ and 10^{-10} . These scalings can be compared with results from simulations shown in Figure 6. Qualitative agreement between the two is evident, including the non-monotonicity of t_d with respect to S , the transition in scaling behaviors as S increases, the deviation between the fastest growing mode and the dominant mode, and the effects of noise amplitude on various quantities. Notably, the model is able to reproduce the crossing of the two $\gamma_d(S)$ curves (highlighted with a green circle in panel (c)), namely, while γ_d is higher for the lower initial noise case at high S , it is the opposite at low S . The reason for the crossing can

be attributed to the mode-stretching effect due to the outflow jets. The stretching effect is more prominent at lower S , as reflected in the larger difference between γ_{max} and γ_d there. Moreover, when S is sufficiently low, the amplitudes of unstable modes cannot grow sufficiently to disrupt the current sheet before being advected out. Therefore, there is a critical Lundquist number S_c below which disruption does not occur. The critical Lundquist number S_c depends on the initial noise amplitude; the lower the noise amplitude is, the higher S_c becomes. Because γ_d becomes very low as S approaches S_c (precisely $\gamma_d \rightarrow \gamma(\pi/L, a_{SP})$), the crossing of $\gamma_d(S)$ curves with different ϵ at low S is simply a consequence of S_c being a decreasing function with respect to ϵ . A similar crossing is also observed between the dominant wavenumber $k_d(S)$ curves, shown in panel (d), because $k_d \rightarrow \pi/L$ as S approaches S_c .

Another notable outcome from the model is the non-monotonicity of γ_d and γ_{max} with respect to S . At low S , the current sheet half-width $a_d \simeq a_{SP}$ at disruption and $\gamma_{max} \sim S^{1/4}$ is an increasing function with respect to S . At high S , γ_{max} becomes a weakly decreasing function with respect to S , and γ_d follows the same trend. Recall that the condition $a_d/L \propto S^{-1/3}$ gives a constant value of γ_{max} independent of S , and $k_{max}L \propto S^{1/6}$. Because γ_{max} is not exactly constant but is weakly decreasing with increasing S , the scalings of a_d and k_{max} are close to, but not exactly $a_d/L \propto S^{-1/3}$ and $k_{max}L \propto S^{1/6}$ (k_d approximately follows the same trend as k_{max} at high S). This weakly decreasing scaling for γ_{max} (or γ_d) at high S has not been observed in numerical simulation yet. The reason could be that the numerical simulations have not been carried out at sufficiently high values of S to reveal this behavior.

We have tested the model with different initial conditions. As an example, Figure 9 shows the scalings with $f_0 = \epsilon(k/k_{min})^{-1}$. Comparing with Fig. 8, the overall trends are rather similar between the two, even though the actual quantitative values can be quite different. This qualitative similarity in scaling relations remains the case for other initial conditions we have tried. Likewise, we have also tested the effect of noise source by setting a floor to the fluctuation amplitude, assumed to be the same as the initial noise $f_0(k)$, and similar scaling relations are obtained.

As we have discussed, the crossings between $\gamma_d(S)$ and $k_d(S)$ curves with respect to different values of initial noise amplitude ϵ is a consequence of S_c being a decreasing function with respect to ϵ . The dependence of S_c on ϵ is fairly weak. For the two types of initial condition we have tried, the critical value S_c as a function of ϵ is shown in Figure 10. In both cases, the initial noise

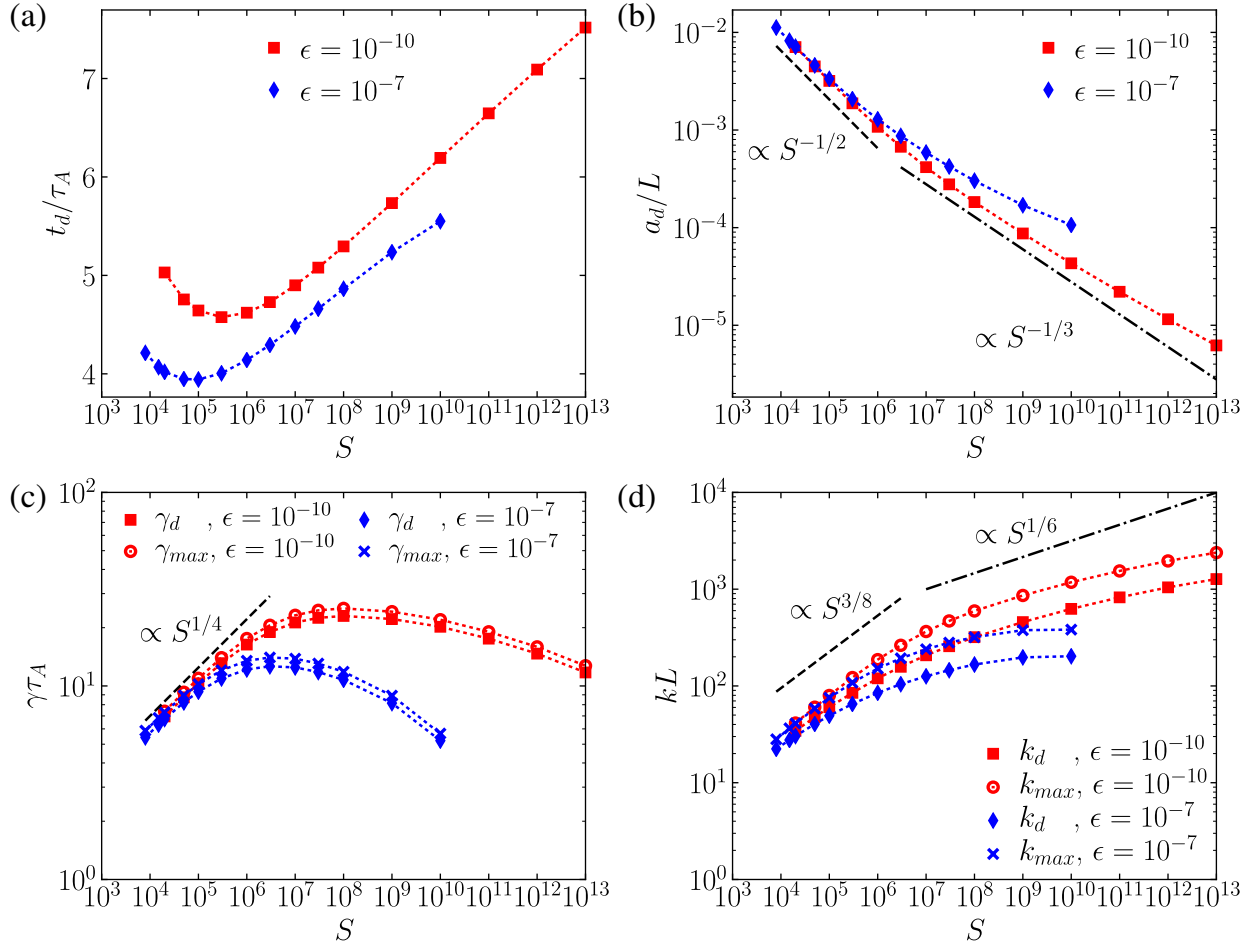


Figure 11. Scalings of t_d , a_d , k_d , and γ_d with respect to S from the model, with the effect of outflow jets turned off.

amplitude ϵ is varied over 25 orders of magnitude but the corresponding S_c changes no more than 3 orders of magnitude.

We can assess the effect of outflow jets by switching off the v'_x terms in Eq. (25). The resulting scalings are shown in Fig. 11. Overall, the scalings are similar to the scalings with outflow in Fig. 8. The most significant differences between the two appear in the low- S regime. In the case without outflow, the difference between γ_d and γ_{max} , as well as that between k_d and k_{max} , become smaller in the low- S regime, as opposed to the case with outflow, where the differences become larger at low S . We also do not find the crossing between curves with different ϵ when outflow is not included in the model. In fact, without the effect of outflow, the critical Lundquist number will be determined by the condition that the longest wavelength mode allowed by the current sheet length L is marginally unstable when the current sheet width is the Sweet-Parker width. This condition gives a critical value $S_c = \pi^2$, which is independent of the

noise amplitude. This value of S_c substantially underestimates the actual value of S_c .

6. FROM DISRUPTION TO NONLINEAR SATURATION AND ONSET OF FAST RECONNECTION

Figure 4(a) shows that the reconnection rate rises rapidly after the disruption time t_d , indicating that current sheet disruption triggers the transition from slow to fast reconnection. Now we have established that the linear growth rate and dominant wavenumber at disruption have nontrivial dependences on various conditions, including the thinning process, the Lundquist number S , the initial noise level and even the spectrum of noise. An important question is, do these conditions affect the reconnection process after the plasmoid instability reaches nonlinear saturation? A full assessment of this question is beyond the present scope and left to future work. To investigate the effect of initial noise level on reconnection rate, we run the two cases S5 and H5 for extended periods well into the nonlinearly saturated phase. The

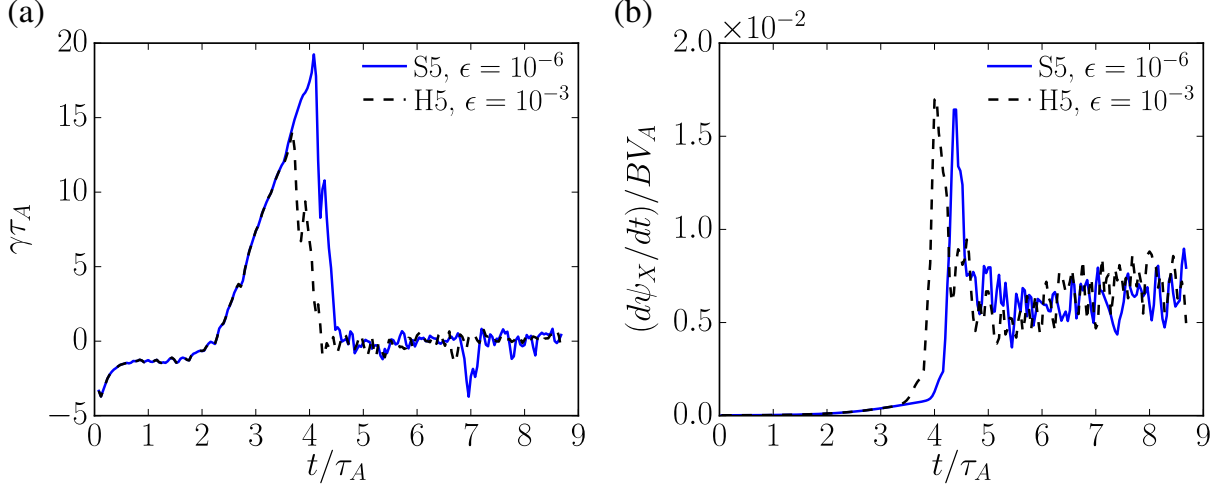


Figure 12. Comparison of time histories of (a) linear growth rate and (b) reconnection rate, for Run S5 (with an initial noise level $\epsilon = 10^{-6}$) and Run H5 ($\epsilon = 10^{-3}$). The initial noise level affects the disruption time and the linear growth rate at disruption, but the reconnection rate after nonlinear saturation remains approximately the same.

resulting time-histories of growth rate and reconnection rate are shown in Fig. 12. Panel (a) shows that current sheet disruption takes place earlier with a lower growth rate in Run H5, where the initial noise level is three orders of magnitude higher than that of Run S5. Because current sheet disruption marks the beginning of onset of fast reconnection, the onset also occurs earlier in Run H5. However, as can be seen from panel (b), the reconnection rates after nonlinear saturation are essentially the same for the two runs. Therefore, we can conclude that reconnection rate after saturation is nearly unaffected by the noise level and the condition at the onset. This conclusion is also in line with the earlier study by Huang & Bhattacharjee (2010), where the dependence of averaged reconnection rate on external forcing amplitude is found to be fairly weak.

From an observational point of view, the period between current sheet disruption and nonlinear saturation is especially interesting. During this period, the outflow profile changes from a nearly monotonic, Sweet-Parker-like profile, to a highly fluctuating profile, as shown in Figure 13(a). Accordingly, the histogram of the outflow profile changes from double-peak-shaped to triangle-shaped, as shown in Figure 13(b). A triangle-shaped histogram is a natural consequence of the outflow profile being highly fluctuating. To understand that, consider an outflow profile of the form $v_x = V_A \sin(\pi x) + v_f \sin(kx)$, where $-1 \leq x \leq 1$ and $k \gg 1$; the first term $V_A \sin(\pi x)$ mimics the Sweet-Parker-like outflow profile, and the second term $v_f \sin(kx)$ mimics short-wavelength fluctuations. If the fluctuation is much smaller than the background, *i.e.* $v_f \ll V_A$, the histogram is double-peak-shaped. On the contrary, if the fluctuation is of the

order of the background, *i.e.* $v_f \simeq V_A$, which is the case in the saturated phase, then the histogram is triangle-shaped. The transition from a double-peak-shaped histogram to triangle-shaped histogram can lead to observable effects through spectroscopy of emission spectral line profiles, because the observed spectral line profile is a convolution of the Doppler-shifted line profile along the line-of-sight direction. For reconnection events with outflows along the line-of-sight direction, the histogram of the outflow profile can be viewed as a proxy for the shape of the line profile. A triangle-shaped line profile has been reported in IRIS (Interface Region Imaging Spectrograph (De Pontieu et al. 2014)) observations of the Si IV line during transition region explosive events (Innes et al. 2015). With the high-cadence mode of IRIS spectrograph, it is possible to observe transitions from a double-peak-shaped line profile to a triangle-shaped line profile in transition region explosive events (Guo 2017). If such transitions can be shown to associate with brightening of emission spectral line, that will provide observational evidence for transition from slow to fast reconnection due to current sheet disruption.

7. DISCUSSION AND CONCLUSION

In this work, we have carried out a detailed study of the development of plasmoid instability in an evolving current sheet and the onset of fast reconnection. We confirm that the Sweet-Parker width can be approached only when the Lundquist number is relatively low. At high values of the Lundquist number, more characteristic of the solar and astrophysical environments, the current sheet breaks apart at a width much larger than the Sweet-Parker width (Pucci & Velli 2014; Uzdensky &

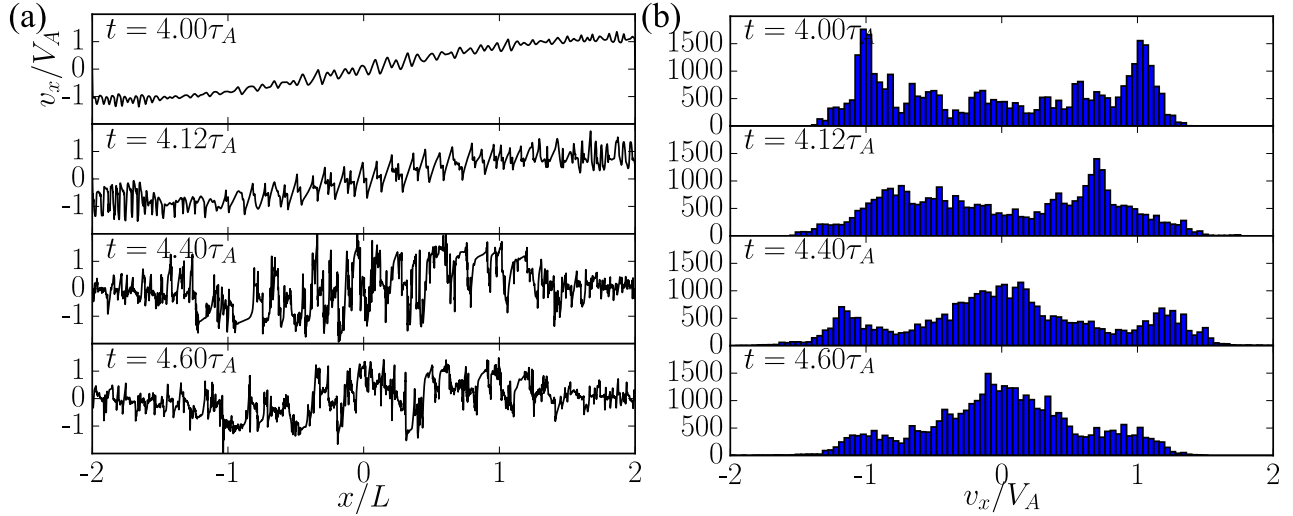


Figure 13. (a) Time sequence of the outflow (v_x) profile along $z = 0$ from disruption ($t = 4\tau_A$) to nonlinear saturation ($t = 4.6\tau_A$) for Run S5. (b) The corresponding histogram of the outflow velocity.

Loureiro 2016; Comisso et al. 2016). However, the level of noise in the system also plays an important role. For a system with lower noise amplitude, the Sweet-Parker width can be approached at a higher Lundquist number and consequently the linear growth rate becomes higher. As such, the linear growth rate and the dominant wavenumber at current sheet disruption exhibit complex dependences on numerous conditions, such as the current sheet evolving process, the Lundquist number, noise level, and even the spectrum of the noise. *Under the condition that the Lundquist number S is the only varying parameter while everything else remains fixed*, we do find that the growth rate at disruption becomes slowly varying with respect to S , as long as S is sufficiently high such that the Sweet-Parker scaling $a_d/L \sim S^{-1/2}$ is no longer valid. Because $a_d/L \propto S^{-1/3}$ is the condition for $\gamma_{max}\tau_A$ to be independent of S , in the high- S regime, the scalings $a_d/L \propto S^{-1/3}$ and $k_d L \propto S^{1/6}$ are approximately realized. While these scaling relations appear to be similar to the suggestion by Pucci & Velli (2014), Pucci & Velli actually imposed a more stringent condition $a_d/L = S^{-1/3}$, leading to the condition that $\gamma_{max}\tau_A \simeq 0.623$ at disruption. Contrary to their suggestion that $\gamma_{max}\tau_A = O(1)$ at disruption, we generally find the linear growth rate at disruption to be substantially higher than $1/\tau_A$. In fact, the time when $\gamma_{max}\tau_A = O(1)$ is approximately when the overall amplitude of fluctuations starts to grow. This hardly comes as a surprise, since the linear growth must be substantial on time scales pertaining to the evolving background for linear theory to be even applicable. In the present case the relevant time scales are the advection and the current sheet evolution time scales, both of the order of τ_A . That means $\gamma_{max}\tau_A > O(1)$ is required. Be-

cause $\gamma_{max} \propto a^{-3/2}$, using the criterion $\gamma_{max}\tau_A \simeq 1$ for disruption will substantially overestimate the disruption half-width a_d , even if the scaling relation $a_d/L \propto S^{-1/3}$ appears to approximately hold; likewise, using the criterion $\gamma_{max}\tau_A \simeq 1$ will substantially underestimate the fastest growing wavenumber k_{max} . For example, using $\gamma_{max}\tau_A \simeq 1$ instead of $\gamma_{max}\tau_A \simeq 20$ as we typically observe in simulations will overestimate a_d by a factor of approximately 7 and underestimate the fastest growing wavenumber k_{max} by a factor of approximately 12. Incidentally, if k_{max} is used to estimate the dominant wavenumber k_d at disruption, as is often assumed, then the error of underestimating k_{max} is partially offset by the fact that the dominant wavenumber k_d is actually smaller than k_{max} .

Our simulation study differs from the earlier study by Tenerani et al. (2015) in an important aspect. In our study the current sheet thinning is self-consistently determined by MHD equations, where Alfvénic jets develop naturally during the process. This thinning process approaches the Sweet-Parker width as the asymptotic state if the plasmoid instability does not set in. On the other hand, Tenerani et al. (2015) employ an extra term in the induction equation to drive the thinning, therefore the asymptotic width is set by the driving term, and there is no significant outflow before the instability sets in. In three out of four simulations (run 1 – run 3) in their study, the asymptotic width is set to be $LS^{-1/3}$, exactly as their theory predicts; in the fourth case (run 4), the asymptotic width is set to be the Sweet-Parker width $LS^{-1/2}$ [see Table 1 in (Tenerani et al. 2015)]. It is particularly revealing to compare their run 1 and run 4, both have exactly the same parameters except the asymptotic width. While the current sheet in run

1 disrupts at $a(\tau_{nl})/L \simeq S^{-1/3}$ (τ_{nl} in their Table 1 is equivalent to t_d in our paper and $a(\tau_{nl})$ is equivalent to a_d in our paper), when the current sheet is allowed to go thinner in run 4, the disruption occurs at an earlier time but the current sheet width is approximately 4 times thinner. It is worth noting that [Tenerani et al. \(2015\)](#) use a fixed value $S = 10^6$ in all their simulations, thereby precluding the possibility of obtaining scaling relations with respect to S .

The phenomenological model presented in Sec. 5 qualitatively reproduces many features obtained from direct numerical simulations, including the non-monotonicity of t_d and changes of scaling behaviors as S increases. It also clarifies why the dominant wavenumber k_d differs from the fastest growing wavenumber k_{max} . An important feature of this model is its capability to predict a critical Lundquist number S_c for a given current sheet evolving process and an initial noise spectrum. The critical Lundquist number S_c is found to have a weak dependence on the noise amplitude. As shown in Fig. 10, for the two types of initial perturbation, the critical value S_c falls in the range from $S_c \simeq 10^3$ to 10^6 for a change in the noise amplitude ϵ over 25 orders of magnitude. This result makes the qualitative argument in ([Huang & Bhattacharjee 2013](#)) more precise, and provides new insight to some empirical knowledge as well as controversy among researchers. The often quoted critical Lundquist number S_c is approximately 10^4 , but this is not a clear-cut value. For example, a critical value S_c as low as 10^3 ([Shen et al. 2013](#)) as well as clean simulations remaining stable up to $S = 2 \times 10^5$ ([Ng & Raghunathan 2011](#)) have been reported. These seemingly conflicting results become comprehensible with the realization that the critical value S_c depends on noise level. Noise can enter a simulation in various ways, such as explicit seeding, discretization errors of numerical schemes, and the implementation of boundary conditions. The simulation setup of [Ng & Raghunathan \(2011\)](#) using a pseudospectral code in a doubly-periodic box without seeded noise is among the cleanest of all scenarios, which accounts for its stability. However, since natural systems always have some noise and the Lundquist numbers are typically much higher, it is unlikely that such systems can remain stable. As we have shown in Sec. 6, the level of noise affects the disruption time, but has a negligible effect on reconnection rate once the instability reaches nonlinear saturation (Fig. 12).

Our results can also be compared with two recent theoretical approaches by [Uzdensky & Loureiro \(2016\)](#) and [Comisso et al. \(2016\)](#). The analysis of [Uzdensky & Loureiro \(2016\)](#) assumes that the current sheet width essentially freezes once the maximum linear growth rate

of all modes that fit into the current sheet (*i.e.* $k > \pi/L$) reaches $1/\tau_{dr}$, where τ_{dr} is the current sheet evolution time scale. Their analysis concludes that the fastest growing mode at that time will be the dominant mode that enters the nonlinear regime and eventually disrupts the current sheet. As such, in the end the criterion of [Uzdensky & Loureiro \(2016\)](#) ($\gamma_{max}\tau_{dr} = 1$) is similar to that of [Pucci & Velli \(2014\)](#) ($\gamma_{max}\tau_A = O(1)$), except that the Alfvénic time scale τ_A in the latter is replaced by τ_{dr} . In the context of the present study, the two criteria are practically the same since $\tau_{dr} \simeq \tau_A$. The time when $\gamma_{max}\tau_A = 1$ is slightly earlier than $t = t_g$ in our simulations. As can be seen from Table 1, the current sheet width evolves quite significantly from $t = t_g$ to $t = t_d$ (the actual difference depends on initial noise level, as does t_d) and consequently the fastest growing wavenumber also changes substantially (see Fig. 4); therefore, the basic assumption of [Uzdensky & Loureiro \(2016\)](#) is not borne out by our simulations. It is worth noting that [Uzdensky & Loureiro \(2016\)](#) use island width w exceeding the current layer width a as the definition of disruption, which is different from our definition of w exceeding the inner layer width δ ; this difference does not affect the discussion here. On the other hand, the analysis of [Comisso et al. \(2016\)](#) starts from a principle of least time, which assumes that the dominant mode at disruption is the one that takes the least time to reach the condition $w = \delta$, for a given initial spectrum $w_0(k)$. The scalings obtained from the principle of least time is very similar to the scalings obtained with our model. The only significant difference is that the effect of outflow is not taken into account in [Comisso et al. \(2016\)](#). The reader can compare Fig. 11(c)(d) (where the effect of outflow is turned off) in this paper and Fig. 1 and Fig. 2 in [Comisso et al. \(2016\)](#) to see the similarities. As we have discussed, the effect of outflow is most pronounced when the Lundquist number is relatively low; therefore, the theory of [Comisso et al. \(2016\)](#) and the model here practically give very similar scalings in the asymptotic limit of large S . For an exponentially thinning current sheet, [Comisso et al. \(2016\)](#) give precisely the logarithmic multiplying factors to the leading order power-law scalings $a_d/L \propto S^{-1/3}$ and $k_d L \propto S^{1/6}$ [*i.e.* the scalings are of the form $\sim S^\alpha (\log f(S, w_0))^\beta$, see their Eqs. (17) and (18)], which account for the deviations from power-laws in Fig. 8(b)(d). It is important to note that these leading order power-law scalings are not universal, as the power indices will be different if the thinning is algebraic rather than exponential [see their Eq. (24)].

We conclude this paper by applying our findings on current sheet disruption to reconnection in the solar at-

mosphere. As a first application, consider the example of post-CME current sheet in (Guo et al. 2013). The current sheet length is estimated as $L \simeq 3 \times 10^{11}$ cm, and the Alfvén speed can be estimated from the speed of moving blobs as $V_A \simeq 2 \times 10^7$ cm/s. Assuming a density of 10^{10} cm^{-3} and a temperature of 10^6 K for typical solar coronal condition, the Lundquist number $S \simeq 3 \times 10^{14}$. The actual disruption condition will depend on the initial noise level, which is not easy to know. If we assume a typical value $\gamma_{\max} \tau_A \simeq 20$ at disruption, that gives an inverse aspect ratio $a_d/L \simeq 1.5 \times 10^{-6}$, *i.e.* $a_d \simeq 4.5 \times 10^5$ cm. Assuming a typical dominant wavenumber $k_d \simeq k_{\max}/4$, we estimate $k_d L \simeq 1500$, and the corresponding inner layer width $\delta \simeq 5000$ cm. Since the inner layer width is much larger than the ion inertial length $d_i \simeq 200$ cm and ion gyroradius $\rho_i \simeq 60$ cm, the resistive MHD model remains valid until disruption. However, nonlinearly the fractal-like cascade will break the current sheet to finer scales. Within the framework of resistive MHD, the cascade will stop when the secondary current sheets become marginally stable (Huang & Bhattacharjee 2010). This condition gives an estimate for the secondary current sheet width $\delta_c \simeq a_{SP} \sqrt{S_c/S}$. Taking a typical value $S_c = 10^4$ yields $\delta_c \simeq 0.1$ cm, which is much smaller than either d_i or ρ_i , therefore collisionless effects must be taken into account at nonlinear saturation (Daughton et al. 2009; Shepherd & Cassak 2010; Huang et al. 2011). As another application, consider the transition region explosive events reported in (Innes et al. 2015). If we estimate the length scale $L \simeq 10^8$ cm and the Alfvén speed $V_A \sim 2 \times 10^7$ cm/s, then $\tau_A \simeq 5$ s. For a temperature 10^5 K and a density 10^{12} cm^{-3} , the Lundquist number in transition region can be estimated as $S \simeq 5 \times 10^9$ based on Spitzer resistivity. Again, assuming $\gamma_{\max} \tau_A \simeq 20$ and $k_d \simeq k_{\max}/4$ at disruption, we obtain $a_d \simeq 5800$ cm, $k_d L \simeq 250$, and $\delta \simeq 400$ cm. Since δ is much greater than $d_i \simeq 20$ cm and $\rho_i \simeq 3$ cm, resistive MHD is applicable at disruption. The secondary current sheet at nonlinear saturation based on resistive MHD is estimated to be $\delta_c \simeq 2$ cm, which is smaller than d_i by an order of magnitude and is comparable to ρ_i . Therefore collisionless effects will not be negligible at nonlinear saturation for anti-parallel

reconnection, but may only be marginally important for component reconnection. How collisionless effects at small scales affect nonlinear saturation in systems with very large L/d_i or L/ρ_i remains an outstanding open question.

Although the present study is restricted to a resistive MHD description, the overall framework can be readily generalized to incorporate other effects. The phenomenological model can be adapted, provided that the linear dispersion relation of tearing instability is available, *e.g.* in visco-resistive (Comisso & Grasso 2016; Comisso et al. 2017) and resistive Hall (Baalrud et al. 2011) regimes. These effects will be considered in future studies. Furthermore, the current sheet evolving process investigated in this study, where the upstream magnetic field remains approximately constant and the current sheet width decreases exponentially in time, is by no means universal, as the current sheet evolution is largely determined by the global configuration of the system. An interesting example is the scenario of reconnection in a layer embedded within a broader outer current sheet, considered by Cassak & Drake (2009). In this scenario, the upstream magnetic field of the embedded layer increases in time; the thinning of the layer, while remains to be studied in detail, may also not be exponential in time. This setup could be employed to investigate how different evolution processes may affect the scalings and further test our phenomenological model. More general situations, where the current sheet length evolves in time, should also be investigated in the future.

Beneficial discussion with Dr. Lijia Guo on IRIS observation is gratefully acknowledged. We thank the anonymous referee for many constructive suggestions. We also thank Dr. Nick Murphy for useful conversations when the paper was under revision. This work is supported by the National Science Foundation, Grant Nos. AGS-1338944 and AGS-1460169, and the Department of Energy, Grant No. DE-SC0016470. Simulations were performed with supercomputers at the Oak Ridge Leadership Computing Facility and the National Energy Research Scientific Computing Center.

REFERENCES

- Alfvén, H. 1943, Arkiv för matematik, astronomi och fysik, 29, 1
- Baalrud, S. D., Bhattacharjee, A., Huang, Y.-M., & Germaschewski, K. 2011, Phys. Plasmas, 18, 092108
- Bhattacharjee, A. 2004, Annu. Rev. Astron. Astrophys., 42, 365
- Bhattacharjee, A., Huang, Y.-M., Yang, H., & Rogers, B. 2009, Phys. Plasmas, 16, 112102
- Biskamp, D. 1993, Nonlinear Magnetohydrodynamics (Cambridge University Press)
- . 2000, Magnetic Reconnection in Plasmas (Cambridge University Press)

- Boyd, J. P. 2001, *Chebyshev and Fourier Spectral Methods*, 2nd edn. (Dover Publications, Inc.)
- Cassak, P. A., & Drake, J. F. 2009, *Astrophys. J. Lett.*, 707, L158
- Cassak, P. A., Shay, M. A., & Drake, J. F. 2005, *Phys. Rev. Lett.*, 95, 235002
- . 2009, *Phys. Plasmas*, 16, 120702
- Comisso, L., & Grasso, D. 2016, *Phys. Plasmas*, 032111
- Comisso, L., Grasso, D., & Waelbroeck, F. L. 2015, *Phys. Plasmas*, doi:10.1063/1.4918331
- Comisso, L., Lingam, M., Huang, Y.-M., & Bhattacharjee, A. 2016, *Phys. Plasmas*, 23, 100702
- . 2017, submitted to *Astrophys. J.*, arXiv:1707.01862
- Coppi, B., Galvao, E., Pellat, R., Rosenbluth, M. N., & Rutherford, P. H. 1976, *Sov. J. Plasma Phys.*, 2, 533
- Daughton, W., Roytershteyn, V., Albright, B. J., et al. 2009, *Phys. Rev. Lett.*, 103, 065004
- Daughton, W., Roytershteyn, V., Karimabadi, H., et al. 2011, *Nature Physics*, 7, 539
- De Pontieu, B., Title, A. M., Lemen, J. R., et al. 2014, *Solar Physics*, 289, 2733
- Fermo, R. L., Drake, J. F., & Swisdak, M. 2010, *Phys. Plasmas*, 17, 010702
- Furth, H. P., Killeen, J., & Rosenbluth, M. N. 1963, *Phys. Fluids*, 6, 459
- Guo, L.-J. 2017, private communication
- Guo, L.-J., Bhattacharjee, A., & Huang, Y.-M. 2013, *Astrophys. J. Lett.*, 771, L14
- Guzdar, P. N., Drake, J. F., McCarthy, D., Hassam, A. B., & Liu, C. S. 1993, *Phys. Fluids B*, 5, 3712
- Huang, Y.-M., & Bhattacharjee, A. 2010, *Phys. Plasmas*, 17, 062104
- . 2012, *Phys. Rev. Lett.*, 109, 265002
- . 2013, *Phys. Plasmas*, 20, 055702
- . 2016, *Astrophys. J.*, 818, 20
- Huang, Y.-M., Bhattacharjee, A., & Sullivan, B. P. 2011, *Phys. Plasmas*, 18, 072109
- Innes, D. E., Guo, L.-J., Huang, Y.-M., & Bhattacharjee, A. 2015, *Astrophys. J.*, 813, 86
- Ji, H., & Daughton, W. 2011, *Phys. Plasmas*, 18, 111207
- Karpen, J. T., Antiochos, S. K., & DeVore, C. R. 2012, *Astrophys. J.*, 760, 81
- Knoll, D. A., & Chacón, L. 2006, *Phys. Plasmas*, 13, 032307
- Kulsrud, R. M. 2005, *Plasma Physics for Astrophysics* (Princeton University Press)
- Lapenta, G. 2008, *Phys. Rev. Lett.*, 100, 235001
- Leake, J. E., Lukin, V. S., & Linton, M. G. 2013, *Phys. Plasmas*, 20, 061202
- Leake, J. E., Lukin, V. S., Linton, M. G., & Meier, E. T. 2012, *Astrophys. J.*, 760, 109
- Loureiro, N. F., Samtaney, R., Schekochihin, A. A., & Uzdensky, D. A. 2012, *Phys. Plasmas*, 19, 042303
- Loureiro, N. F., Schekochihin, A. A., & Cowley, S. C. 2007, *Phys. Plasmas*, 14, 100703
- Loureiro, N. F., & Uzdensky, D. A. 2016, *Plasma Phys. Control. Fusion*, 58, 014021
- Lynch, B. J., Edmondson, J. K., Kazachenko, M. D., & Guidoni, S. E. 2016, *Astrophys. J.*, 826, 43
- McKechan, D. J. A., Robinson, C., & Sathyaprakash, B. S. 2010, *Class. Quantum Grav.*, 27, 084020
- Murphy, N. A., Young, A. K., Shen, C., Lin, J., & Ni, L. 2013, *Phys. Plasmas*, 20, 061211
- Ng, C. S., & Ragunathan, S. 2011, in *ASP Conference Series*, Vol. 444, *Numerical Modeling of Space Plasma Flows: ASTRONUM-2010*, ed. N. V. Pogorelov, E. Audit, & G. P. Zank (Astronomical Society of the Pacific), 124–129
- Ni, L., Ziegler, U., Huang, Y.-M., Lin, J., & Mei, Z. 2012, *Phys. Plasmas*, 19, 072902
- Oishi, J. S., Low, M.-M. M., Collins, D. C., & Tamura, M. 2015, *Astrophys. J. Lett.*, 806, L12
- Parker, E. N. 1957, *J. Geophys. Res.*, 62, 509
- Priest, E. R., & Forbes, T. 2000, *Magnetic reconnection : MHD theory and applications* (Cambridge University Press)
- Pucci, F., & Velli, M. 2014, *Astrophys. J. Lett.*, 780, L19
- Rutherford, P. H. 1973, *Phys. Fluids*, 16, 1903
- Schindler, K. 2007, *Physics of Space Plasma Activity* (Cambridge University Press)
- Shen, C., Lin, J., Murphy, N. A., & Raymond, J. C. 2013, *Phys. Plasmas*, 20, 072114
- Shepherd, L. S., & Cassak, P. A. 2010, *Phys. Rev. Lett.*, 105, 015004
- Shibata, K., & Tanuma, S. 2001, *Earth Planets Space*, 53, 473. www.terrapub.co.jp/journals/EPS/abstract/5306/53060473.html
- Sironi, L., Giannios, D., & Petropoulou, M. 2016, *Monthly Notices of the Royal Astronomical Society*, 462, 48
- Sweet, P. A. 1958, in *Electromagnetic phenomena in cosmical physics*, ed. B. Lehnert, Vol. 6 (Cambridge University Press), 123–134
- Tajima, T., & Shibata, K. 1997, *Plasma Astrophysics* (Addison Wesley)
- Takamoto, M. 2013, *Astrophys. J.*, 775, 50
- Tenerani, A., Velli, M., Rappazzo, A. F., & Pucci, F. 2015, *Astrophys. J. Lett.*, 813, L32
- Uzdensky, D. A., & Loureiro, N. F. 2016, *Phys. Rev. Lett.*, 116, 105003
- Uzdensky, D. A., Loureiro, N. F., & Schekochihin, A. A. 2010, *Phys. Rev. Lett.*, 105, 235002

Yamada, M., Kulsrud, R., & Ji, H. 2010, *Rev. Mod. Phys.*,
82, 603

Zweibel, E. G., & Yamada, M. 2009, *Annu. Rev. Astron.*
Astrophys., 47, 291
—. 2016, *Proc. R Soc. A*, 472, 20160479